Review of
Scientific Instruments

AIP
Publishing

RESEARCH ARTICLE | JUNE 06 2025

# The infrared imaging video bolometer at Wendelstein 7-X

G. Partesotti ✉ ; G. A. Wurden ; F. Reimold ; B. J. Peterson ; F. Federici ; K. Mukai ;
K. A. Siever; J. von Miller; D. Zhang ; A. Demby; W7-X Team

*Rev. Sci. Instrum.* 96, 063503 (2025)
https://doi.org/10.1063/5.0261413

Review of
Scientific Instruments

ARTICLE

pubs.aip.org/aip/rsi

# The infrared imaging video bolometer at Wendelstein 7-X

Cite as: Rev. Sci. Instrum. 96, 063503 (2025); doi: 10.1063/5.0261413
Submitted: 30 January 2025 • Accepted: 13 May 2025 •
Published Online: 6 June 2025

G. Partesotti,[1,a)] G. A. Wurden,[2] F. Reimold,[1] B. J. Peterson,[3] F. Federici,[4] K. Mukai,[3] K. A. Siever,[1] J. von Miller,[1] D. Zhang,[1] A. Demby,[5] and W7-X Team[b)]

## AFFILIATIONS

[1] Max-Planck Institute for Plasma Physics, Greifswald, Germany
[2] Los Alamos National Laboratory, Los Alamos, New Mexico 87545, USA
[3] National Institute for Fusion Science, Toki, Japan
[4] Oak Ridge National Laboratory, Oak Ridge, Tennessee 37830, USA
[5] University of Wisconsin-Madison, Madison, Wisconsin 53706, USA

[a)] **Author to whom correspondence should be addressed:** gabriele.partesotti@ipp.mpg.de
[b)] O. Grulke *et al.*, Nucl. Fusion **64**, 112002 (2024).

## ABSTRACT

The radiated power distribution is a crucial aspect of heat transport, heat load mitigation, and plasma exhaust performance. An imaging video bolometer camera has been installed to measure the plasma radiated power in the divertor region of the Wendelstein 7-X (W7-X) stellarator. This diagnostic offers a wide-angle ($40^\circ \times 68^\circ$) sampling of the plasma volume in both the poloidal and toroidal directions. The field-of-view is covered with a large number (>500) of bolometer channels, providing imaging capability. The diagnostic design is introduced here together with its data analysis procedure. A set of laboratory experiments is performed to assess the thermal properties of the gold absorber foil and their spatial uniformity. Following installation, a heat source originating from the inertially cooled front of the diagnostic is identified and filtered out. The discharge data indicate a satisfactory signal-to-noise ratio as well as spatiotemporal resolution. These represent the first toroidally resolved images of the line-integrated radiated power in the W7-X island divertor. The diagnostic was then upgraded with a thinner platinum absorber and adjusted mirrors. Early data from the most recent experimental campaign employing the upgraded design show a considerable improvement in the diagnostic performance with more bolometer channels (>1400), extended coverage, and increased spatial resolution.

## I. INTRODUCTION

In current day fusion devices, a large fraction of the plasma stored energy can be efficiently dissipated through radiation.[1] Therefore, the correct assessment of plasma emission is a key component for both physics studies and machine operation. In a tokamak, axisymmetry of local plasma parameters is often observed.[2] On the other hand, in helical devices—such as stellarators—the plasma emissivity (i.e., radiated power density) can be highly asymmetric and, therefore, harder to diagnose properly.[3,4]

Radiated power measurements are routinely performed by bolometer diagnostics. These are based on the exposition of an absorber element to the plasma radiation. By measuring the temperature change on the absorber, the absorbed power can be retrieved.[5] The absorber is typically a thin, radiation-hard, C-coated metal foil (usually Au) of known thermal properties.[6] In the most common design (i.e., resistive bolometer detectors), the absorber is placed in thermal contact through an electrically insulating layer with a resistor (often Pt meanders). Its electrical resistivity is then monitored through a Wheatstone bridge. The bridge signal indirectly provides a measurement of the absorber temperature and, therefore, the incident power.[7] These detectors can ultimately be arranged in fan-shaped arrays inside a pinhole camera to define multiple collimated lines-of-sight (LoS), providing spatially resolved information.[8]

A different approach from the conventional resistive one is taken by the InfraRed (imaging) Video Bolometer (IRVB) diagnostic. In an IRVB, the foil temperature measurement is performed by recording the thermal emission from the back (non-plasma-facing) side of the bolometer foil with a high-resolution infrared (IR) camera.[9,10] The foil is mounted on a metallic frame and placed between the pinhole and the optical path of the camera, ensuring structural stability as well as a uniform temperature of the heat sink in thermal contact with the foil edge (frame thermal mass is much larger than foil thermal mass). To take advantage of the imaging capability of the observing optics, a larger bolometer foil can be employed. The standard IRVB foil size is 70 × 90 mm$^2$, which allows a much broader collection angle compared to the 4 × 1.5 mm$^2$ of a resistive detector element.[5,6] A wide viewing angle is highly beneficial in fusion devices, as it provides extended and continuous coverage of the plasma volume both in the poloidal and toroidal directions from one viewpoint alone. In tokamaks, with the assumption of axisymmetry, one IRVB diagnostic with a tangential view can be sufficient to image the plasma poloidal cross section and perform tomographic inversions of the 2D radiation distribution.[11–15] At the Large Helical Device (LHD), four separate IRVBs were combined[16] to achieve 3D tomography of the radiating structure.[3]

Bolometer diagnostics of the IRVB type have already been tested experimentally on several tokamak machines (JT-60U,[17] ADITYA-U,[18] SST-1,[19] Alcator C-Mod,[20] KSTAR,[21] and MAST Upgrade[15]), as well as helical (LHD[10] and Heliotron J[22]) and mirror fusion devices (GAMMA 10/PDX[23]), although more conceptual designs exist (NSTX-U[24] and JT-60SA[11]). In the large W7-X stellarator, an IRVB has been installed to characterize the plasma radiated power in the island divertor.[25] This work aims to introduce the imaging bolometer diagnostic at W7-X and present the first experimental results.

First, the IRVB design at W7-X is described in Sec. II. Section III follows by introducing the measurement principle, while Sec. IV discusses data interpolation from the camera FoV onto the bolometer foil surface. Then, the thermal properties of the foil are calibrated in Sec. V. The diagnostic operation is reported in Sec. VI, where the data analysis procedure is described and applied to discharge data from the past experimental campaign. The section concludes with the upgraded IRVB design and early data from the most recent experimental campaign.

## II. THE IRVB DESIGN AT W7-X

A first iteration of the imaging bolometer was installed at W7-X in 2021. The optics, IR camera, and endoscope for the IR imaging setup were repurposed from the thermography system that monitored the now retired W7-X scraper element.[26,27] This iteration was operational during the OP2.1 campaign, which took place in the years 2022–2023 and is referred to as the "OP2.1" in the text.

A circular steel cap is added to the endoscope front to house the bolometer foil and define the pinhole geometry.[28] A computer-aided design (CAD) model of the endoscope front is illustrated in Sec. I. The pinhole and foil (yellow) are separated by a 55 mm distance perpendicular to the foil surface. A series of steel baffles (red) coated with an $Al_2O_3/TiO_2$ layer is mounted in between to provide absorption of stray microwaves[29] and suppress optical reflections inside the pinhole camera (similar to blackening). On the baffle that is closest to the foil surface, a fine metallic wire mesh (blue) is attached to further shield the foil from microwave radiation (5% transmission factor, 53% optic throughput).[8,30] Neither active cooling nor shutter functionality is implemented in this design.

As an absorber element, we use a 5.0 $\mu$m thick 70 × 90 mm$^2$ free-standing gold foil produced by Nilaco mounted on a 9 mm thick copper frame (orange), as shown in Fig. 1. Several locations on the frame are perforated with venting holes to avoid pressure differences between the plasma-facing side and the camera-facing side of the foil. The foil is coated on both sides with a thin graphite layer by chemical vapor deposition to increase its absorption coefficient. This is similar to the blackening process typically applied to resistive metal foil bolometers.[31] The thickness of the coated layer is expected to be on the order of 200 nm. Thicker layers were found to reduce the foil sensitivity while providing little improvement to the absorption coefficient.[32]

After being clamped in the copper frame, the exposed foil area is 66 × 86 mm$^2$. We identify these dimensions in the 2D plane of the foil surface as the foil height and width, respectively, or vertical direction $y$ and horizontal direction $x$ throughout the paper (white arrows in Fig. 1).

The pinhole is a square aperture of size 5 × 5 mm$^2$ machined into the cap with a 30° beveled edge at the position indicated in Fig. 2. Its location is not centered on the foil central axis but is instead displaced by 30 mm in the $-x$ direction and 20 mm in the $+y$ direction. This is performed to direct the FoV, shown in orange in Fig. 3, toward the divertor target plates. To protect the more sensitive (not radiation-resistant) components from the fusion environment, the camera (green) and acquisition electronics are placed further away from the plasma vessel.[32,33] As shown in pink in Sec. I, four Al-plated parabolic mirrors (75 mm diameter, 228 mm focal length) are enclosed in the endoscope front. These collect blackbody emission from the foil and focus it on the camera lens at the endoscope back.

We employ a Teledyne FLIR SC8303HD high-resolution and high-speed infrared camera with an active spectral range of 3.0–5.0 $\mu$m.[26] This model is operated in a sub-windowed mode of 512 × 512 pixels at a frame rate of 200 Hz (the full-window regime

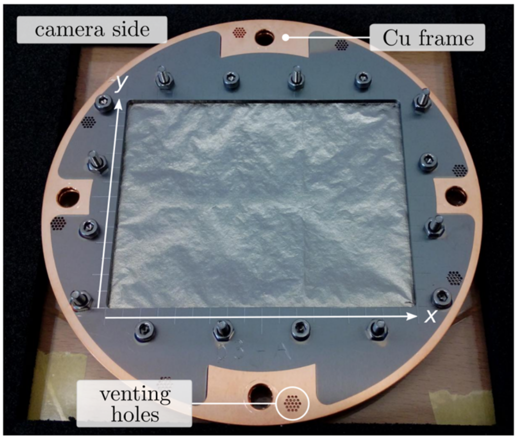

**FIG. 1.** Photograph of the C-coated Au bolometer foil mounted on the Cu frame. White arrows identify the foil reference frame and the location of the venting hole.

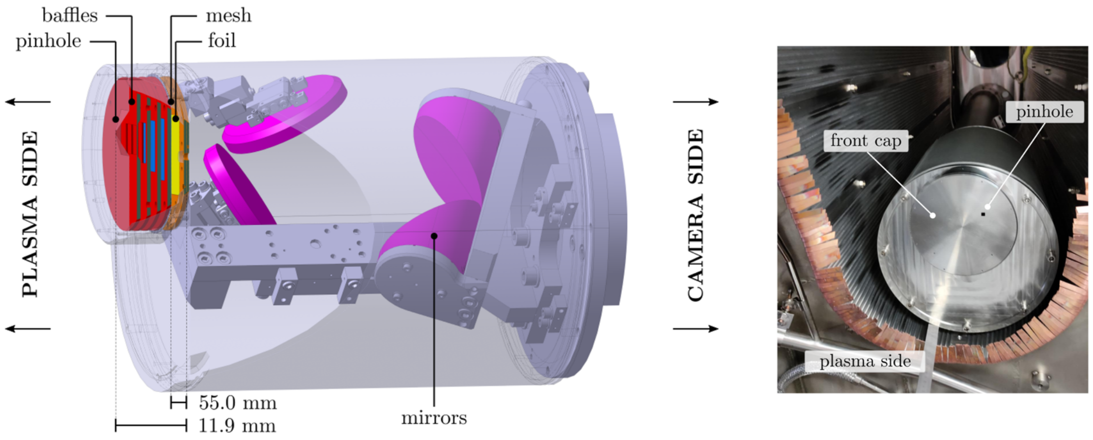

(a) CAD model of the endoscope front

(b) Installed endoscope

**FIG. 2.** (a) CAD model of the IRVB endoscope front. From left (plasma side) to right (camera side): pinhole, microwave baffles (red), microwave mesh (blue), bolometer foil (yellow) mounted on the copper frame (orange), and IR mirrors (pink). (b) Photograph of the endoscope front after installation in the diagnostic port.

would be 1344 × 784 pixels at 125 Hz). Inside the camera, the Focal Plane Array (FPA) sensors are cooled by an integrated Stirling cryocooler. The camera and acquisition electronics are enclosed in an air-cooled iron box inside the torus hall to avoid magnetic field interference on the camera focusing or cooling systems.[34] An uncoated IR-transmitting sapphire vacuum window at the cryostat interface provides the necessary separation between the low-pressure fusion environment and the atmospheric pressure at which the IR camera operates (IR transmittance is 60–88% in the range of interest). The window, made by Guild Optics (Vermont, USA), mounts a custom Helicoflex metal vacuum seal. In the future, a multilayer antireflection coating should be applied to the IR window to increase its transmittance factor. A CAD drawing of the current system is depicted in Fig. 3.

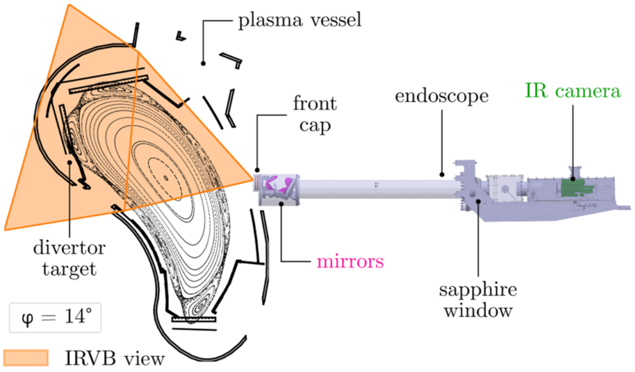

**FIG. 3.** CAD drawing of the imaging bolometer system with the main components highlighted. IR emission from the foil backside (inside the steel cap) is collected by the IR mirrors (pink) and delivered to the IR camera (green). The FoV projected in the poloidal plane (orange) at $\varphi = 14°$ is superimposed on a Poincaré plot of the W7-X standard magnetic field configuration.

The used diagnostic port is AEK51, situated near the outboard midplane. The port exit faces the low-iota target section of the upper divertor unit of sector five, at a toroidal angle $\varphi = 14°$ within the stellarator-symmetric magnetic module ($\Phi = 302°$ in the machine reference system). A cross-sectional view of the machine at this toroidal angle is shown on the left-hand side of Fig. 3, with the IRVB view cone (orange) collapsed on the $(R, z)$ poloidal plane.[35] The collection angle is 40° in the poloidal direction and 68° in the toroidal direction. The three-dimensional extent of the IRVB FoV can be better visualized in Fig. 4. Only the upper portion of the plasma volume is covered by the IRVB. In the toroidal direction, the IRVB detection volume spans the range $\varphi = 0°–20°$ ($\Phi = 288°–308°$). Therefore, the total toroidal collection angle of the IRVB is $\Delta\varphi = 20°$.

Figure 5 shows a rendered image of the machine wall projected on the IRVB foil reference frame. Axis directions are inverted with respect to the $xy$ plane of Fig. 1 to remove the pinhole inversion effect (the image being displayed upside-down and reversed left-to-right). The projection was generated using the Calcam software[36] to simulate the FoV and collimation of the IRVB pinhole camera. A horizontal ($x$ direction) movement in this foil view corresponds to a toroidal movement inside the machine. A vertical movement ($y$ direction) corresponds to a poloidal movement, with the $z$ axis pointing upward. In standard magnetic field configuration, the magnetic axis crosses the lower side of the picture horizontally (white line), with the positive field direction pointing from left to right (counterclockwise when viewing the torus from above).[37] The $\varphi = 14°$ plane (teal) falls on the right-hand side. Sightlines intersecting with the vertical target section occupy the center portion of the foil image, while the horizontal target region appears on the upper side.

To extract the spatially resolved power information, the surface of the bolometer foil can be discretized into a given number of pixels to define individual bolometer lines-of-sight (LoS). This way it is possible to attain a very large number of bolometer channels from a single, large foil. The bolometer channels are sometimes called

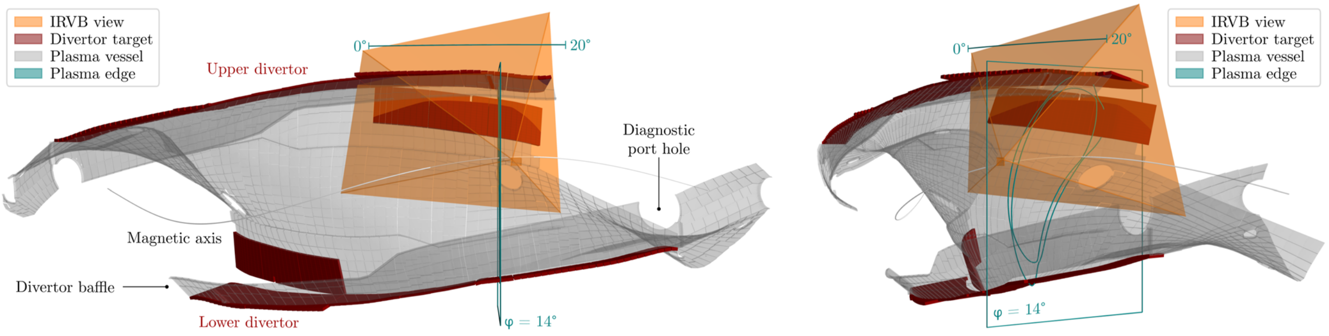

(a) Front view of IRVB (b) Side view of IRVB

**FIG. 4.** Geometry of the IRVB diagnostic viewed (a) from the front and (b) from the side. The FoV (orange) is superimposed on a three-dimensional render of the main W7-X vessel (semitransparent gray) and divertor target (red) components. A plot of the standard magnetic island geometry in the $\varphi = 14^\circ$ plane (teal) and the magnetic axis (white) is included for reference.

*macropixels* to distinguish them from the IR camera channels, often called *micropixels*. The number of bolometer channels is determined by a trade-off between spatial resolution and Signal-to-Noise Ratio (SNR). This in turn depends on how many IR camera channels are binned together into each bolometer channel to form the bolometer signal, the IR camera specs, and the viewing geometry. With a state-of-the-art IR camera, several hundred to a thousand bolometer channels can be achieved. Hence, the IRVB approach significantly reduces the required port space and cost per bolometer channel compared to the traditional resistive bolometers while maintaining a similar SNR and spatial resolution.[38] We discretize the surface using a regular square grid with 26 divisions in the $x$ direction and 20 divisions in the $y$ direction. This yields a $20 \times 26 = 520$ square mesh of $l_{bol} = 3.3 \times 3.3$ mm$^2$ size. The spatial resolution of each bolometer channel (distance between neighboring central LoSs) is ~25 mm on the plasma side near the pinhole and 75 mm on the far side near the target plates.

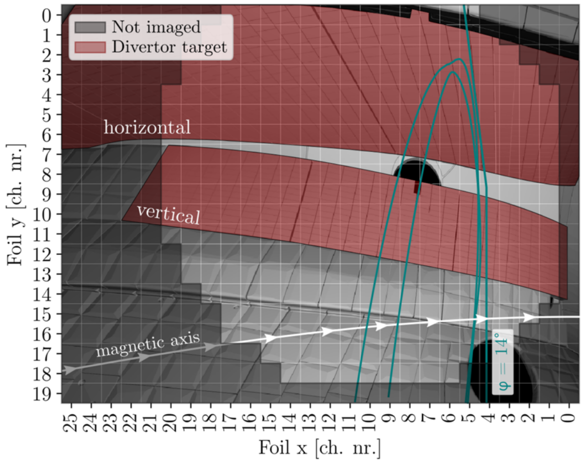

**FIG. 5.** Wall components from Fig. 4 projected onto the foil reference frame. Bolometer channel numbers in the $x$ and $y$ directions (as indicated in Fig. 1) are noted on the axes. The foil area that is not imaged by the mirrors is shaded a darker color.

Only a limited portion of the available foil surface can be acquired in this setup due to the large magnification provided by the IR mirrors (see Sec. IV). Bolometer channels that fall outside the area imaged by the mirrors are shaded with a darker color in Fig. 5. Since the IR signal from this area is not collected, the corresponding bolometer LoS is effectively not available. With this optical setup, only 239 bolometer channels out of 520 are useable (46%).

In the foil view of Fig. 5, the pinhole is located above the bottom-right corner. We express the optical throughput offered by the pinhole to each bolometer channel in terms of its etendue value $e$ [m$^2$ sr][37,39]

$$e = \Omega\, A_P \cos(\beta) = \frac{l_{bol}^2 \cos(\alpha)}{d^2} A_P \cos(\beta), \qquad (1)$$

with $\Omega$ solid angle subtended by the pinhole to the bolometer channel, $A_P$ pinhole area, and $\beta$ angle between the pinhole axis and the line connecting the pinhole center and bolometer channel (central LoS). The solid angle $\Omega$ itself depends on the foil area covered by the bolometer channel $l_{bol}^2$, its distance to the pinhole $d$, and the angle $\alpha$ between the normal to the foil surface and the central LoS. Figure 6(a) shows the spatial variation of $e$ calculated across the foil. Since the incident power signal tends to peak in the region where the etendue is the highest, a regularization will be applied in Sec. VI to remove this pinhole dependence from the power data.

Finally, we can visualize the intersection of each LoS with the plasma by computing the intersection length $d_{LoS}$ (along the central sightline) and volume $V_{LoS}$. The plasma volume is approximated with a separatrix surface extended to enclose the islands.[39] Different coil current configurations will produce different magnetic field geometries and, therefore, different sets of $d_{LoS}$ and $V_{LoS}$. Figures 6(b) and 6(c) show their respective distribution on the foil for the standard W7-X magnetic field configuration.[40] Most notably, both drop to zero on the upper right corner of the foil above the horizontal target plate (indicating no crossing with the plasma), and they are not uniform in the horizontal (toroidal) direction. This will become relevant when interpreting experimental measurements in Sec. VI.

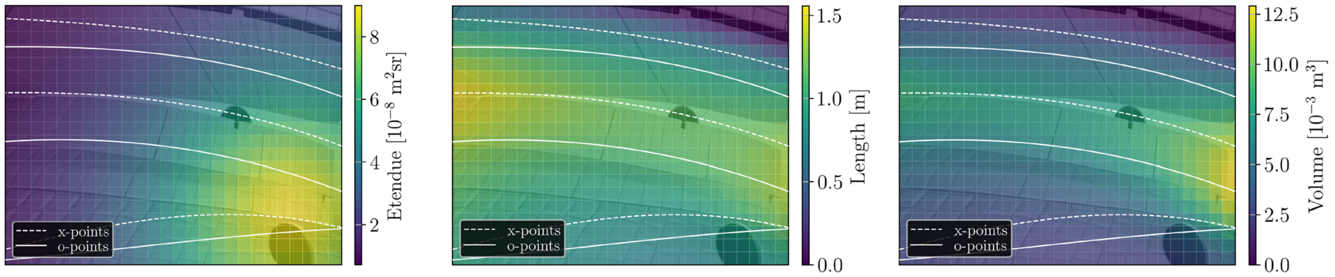

(a) LoS etendue, $e$

(b) LoS length, $d_{LoS}$

(c) loS volume, $V_{LoS}$

**FIG. 6.** Distribution of relevant geometrical parameters on the foil, calculated per bolometer channel: (a) etendue, (b) intersection length with the plasma, and (c) intersection volume with the plasma. The latter two are calculated for the W7-X standard magnetic field configuration. The island X- (dashed) and O-points (solid) traces in this geometry are projected onto the foil view with white lines.

## III. MEASUREMENT PROCEDURE

Data analysis of the IRVB diagnostic at W7-X involves several steps: correction of non-uniformities in the raw camera image, interpolation of the IR camera count data to the foil reference frame, conversion from counts to temperature, and inference of the incident power. Our first step in the data analysis procedure is mitigating the effects of different IR detector sensitivities by applying a Non-Uniformity Correction (NUC). This is performed by blocking the optical path of the IR camera with a flat NUC plate of even emissivity and temperature. During operation, occasional drifts in the detector readings can occur. An internal NUC flag mechanism is periodically activated to update the correction.

The counts on the bolometer channels are then converted to units of equivalent surface temperature with temperature conversion factors that are calibrated in dedicated laboratory experiments. The calibration is performed in air with a thermocouple on a precision blackbody emitter that offers an isotropic emissivity surface over a range of 20–300 °C. It is calculated inside a limited area in the center of the camera FoV and then applied to all IR camera channels. This blackbody source provides a much wider span of temperatures, but only above the useful range for the IRVB foil (typically <10 °C above ambient temperature). In comparison, using a warmed-up/refrigerated NUC plate samples a range that spans above and below it.[15] The blackbody emitter also allows us to precisely control the source temperature, avoiding the uncertainty given by letting it equilibrate to room temperature naturally.[20]

Using the FLIR internal software calibration tool, the conversion is approximated with polynomial functions, for which we compute 10 polynomial coefficients. Since these depend on the acquisition settings of the IR camera (e.g., integration time and frame rate), a different set is needed for different camera presets. The software calibration tool also takes into account environmental conditions that can affect the readings, such as lens temperature or FPA temperature. The transmission of the sapphire IR window was included.

Having obtained the time-resolved data of the temperature distribution $T$ on the foil, the incident power $p_{abs}$ absorbed by each bolometer channel can be inferred. Individual bolometer channels are not independent in the IRVB concept. A thermal diffusion equation needs to be applied to calculate heat transport on the foil and extract the incident power information. Since the IRVB foil is sufficiently thin, heat transport through the foil thickness is assumed to be instantaneous. Hence, the analysis is reduced from 3D to a 2D problem on the foil surface. This is solved numerically by applying a Finite Difference (FD)[10] approach to estimate the time-resolved power influx and outflux to and from the corresponding bolometer channel. In the calculation, three components of the power flux are considered: diffusion with neighboring regions $p_{\nabla^2 T}$, losses due to thermal radiation $p_{BB}$, and changes in temperature (thermal energy) over time $p_{\dot{T}}$. The sought $p_{abs}$ $[\mathrm{Wm}^{-2}]$ information is simply given by the sum of all these individual contributions

$$\begin{aligned} p_{abs} &= p_{\nabla^2 T} + p_{BB} + p_{\dot{T}}, \\ p_{\nabla^2 T} &= -\frac{1}{S}\,\nabla^2 T, \\ p_{BB} &= 2\,\varepsilon\,\sigma_{SB}\,\left(T^4 - T_0^4\right), \\ p_{\dot{T}} &= \frac{1}{\kappa\,S}\frac{\mathrm{d}T}{\mathrm{d}t}, \end{aligned} \tag{2}$$

with foil thickness $t_f$, sensitivity $S$ $[\mathrm{KW}^{-1}]$, thermal diffusivity $\kappa$ $[\mathrm{m}^2\ \mathrm{s}^{-1}]$, emissivity $\varepsilon$, Stefan–Boltzmann constant $\sigma_{SB}$ $[\mathrm{Wm}^{-2}\ \mathrm{K}^{-4}]$, and ambient temperature $T_0$. Here, we have defined the foil sensitivity as $S = \frac{1}{k\,t_f}$,[10] where $k$ is the thermal conductivity $[\mathrm{Wm}^{-1}\ \mathrm{K}^{-1}]$. This is akin to the sensitivity of resistive metal foil bolometers.[7,37,41,42] These components can be multiplied by the surface area of the bolometer channel $l_{bol}^2$ to express them in units of power instead of power per surface area. All the equations used for the FD model and their derivation are noted in Appendix A. An application of the FD approach to synthetic data is reported in Appendix B to delucidate the limits of the analysis scheme.

Similar to the resistive bolometer concept, the inferred absorbed power is unique and exact as long as the thermal properties of the detector are known. More specifically, three foil thermal properties are required to infer the absorbed power of IRVB: $\varepsilon$, $\kappa$, and $S$. $\varepsilon$ controls the absorption and cooling efficiency of the foil, $\kappa$ controls the spatial localization of the temperature features, and $S$ controls the magnitude of the temperature response. These values will vary for different bolometer foils and within the foil. Hence, the requirement for a calibration procedure, discussed later in Sec. V.

## IV. INTERPOLATION TO FOIL REFERENCE FRAME

Before solving for the incident power, the measured count data need to be assigned to the respective bolometer channel. Our view on the foil is mediated by the four Al-plated mirrors introduced in Sec. II. These deflect, collimate, and focus the infrared radiation from the foil onto the camera. The resulting foil image is distorted and partially cropped in the camera view, as can be seen in Fig. 8(a), which reports a typical NUC-corrected measurement of counts acquired with the IR camera during a plasma discharge with $P_{rad} = 1.0$ MW of total plasma radiated power. The imaged portion of the foil (blue) lies in the center of the view (dashed white line). Only a small part of one edge of the Cu frame (red) with one of the clamping bolts is visible on the upper right-hand side.

In addition to the optical distortions, the foil image acquired by the IR camera is flipped upside down and left to right and rotated by 45° with respect to the real picture of the foil backside emission. These optical effects are measured by observing a calibration plate [Fig. 7(a)] with known reference marks through the same optical system used in the experiment [Fig. 7(b)]. A bivariate spline interpolation is used to transform points from the coordinate system of the camera [Fig. 7(c)] to the corresponding point in the reference frame of the foil [Fig. 7(d)] and correct for optical effects. One bolometer channel is highlighted in green to better understand the transformation between the two.

Points in the proximity of the optically cropped borders of the mirrors exhibit considerable warping and bending, rendering the interpolation unreliable. Within these blind spots, the interpolation function is not properly defined. We identify a trusted area by defining a contour line (red) on the calibration plate snapshot of Fig. 7(b). Values outside this accepted region (teal) are discarded in the signal analysis. This selection is applied to IRVB measurements plotted in the foil reference frame. We can see how the four foil corners are cropped out of the camera view, along with three out of the four foil edges. Note that the edges of the bolometer grid are compressed in Fig. 7(c), giving the false impression that the trusted area extends to three of the four sides of the foil (instead of one).

The count data measured by the camera are mapped from the grid of IR camera channels to the grid of bolometer channels using a 2D mesh interpolation routine. First, the area of overlap between each IR camera channel and every bolometer channel is computed. Then, a count value is assigned to each bolometer channel by averaging together all the count values of the corresponding overlapping IR channels. To conserve the spatial count information, a weighted average is used with the weights being the surface area of the intersection between each IR channel and the bolometer channel under consideration. With a sufficient number $N$ of IR camera channels averaged per bolometer channel, this averaging reduces random noise fluctuations as the IRVB sensitivity is proportional to $\sqrt{N}$.[33] Figure 8(b) reports the example measurement previously introduced in Fig. 8(a) interpolated in this way.

We overlap the IR camera channel grid [axes of Fig. 7(c)] with the mapped bolometer channel grid [black lines in Fig. 7(c)] and compute the number of IR camera channels per bolometer channel, finding an average number $N = 425$. The barrel distortion effect near the center of the camera image magnifies the view on the bolometer channels in the upper right corner of the foil, which are imaged by $N > 500$ IR detectors. Conversely, bolometer channels in the lower left-hand side are compressed and overlap with $N > 300$ IR camera channels. On average, $N = 425$, and the foil area covered by one IR camera channel is $A_{IR} = 0.0256$ mm$^2$ ($l_{IR} = 0.16$ mm), compared to a much larger $A_{bol} = 10.89$ mm$^2$ for the bolometer channels. After the binning process, the Noise Equivalent Temperature (NET) of the signal is reduced from an initial $\sigma_{IR} = 70$ mK on the camera data to about $\sigma_{bol} = 7$ mK on the bolometer data.

## V. CALIBRATION OF THE FOIL THERMAL PROPERTIES

In this section, the calibration parameters are assessed in terms of their magnitude and uniformity across the foil surface. Some common sources of non-uniformity in the calibrated values are varying foil thickness, inhomogeneity of the coating, and surface defects (e.g., pinholes, wrinkles, tears, and delamination). For example, the foil surface not being ideally flat (as visible in Fig. 1) could produce some degree of variability in the spatial response of the detector.

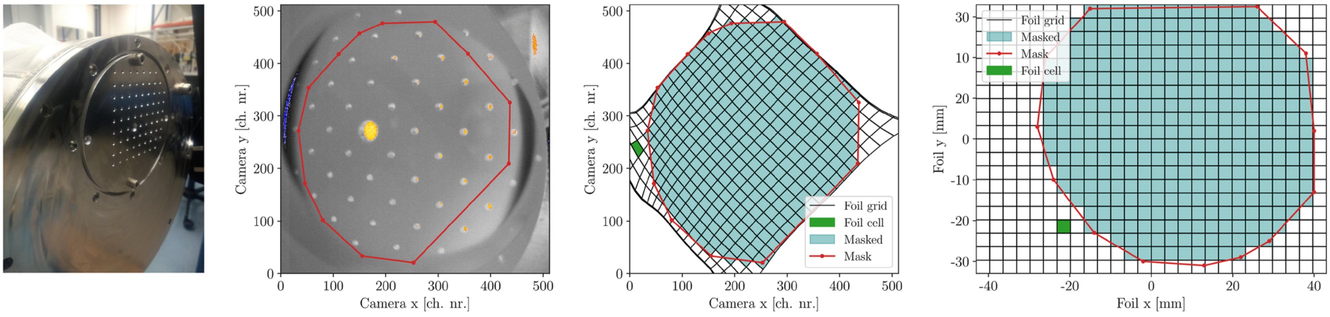

(a) Calibration plate (b) Calibration image (c) IR camera view (d) Foil backside view

**FIG. 7.** (a) Photo of the calibration plate mounted on the endoscope front, and (b) depicted using the IR camera through the optics. Using a bivariate spline interpolation, a mapping between points on the foil surface in (c) the camera image and (d) the foil coordinate system is calculated. The contour used to select the useable bolometer channels is plotted as a red solid line contour. Selected points are indicated with a light blue fill. The same bolometer channel is highlighted in green in (c) and (d) for reference.

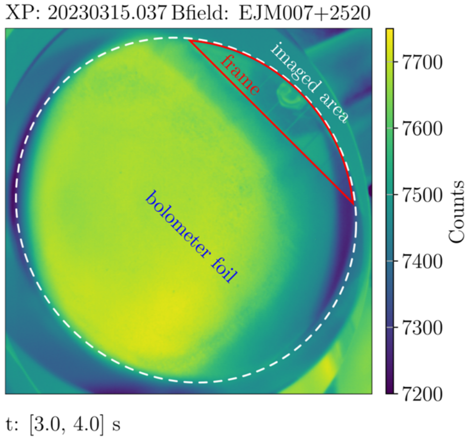

(a) Raw counts measured by IR camera

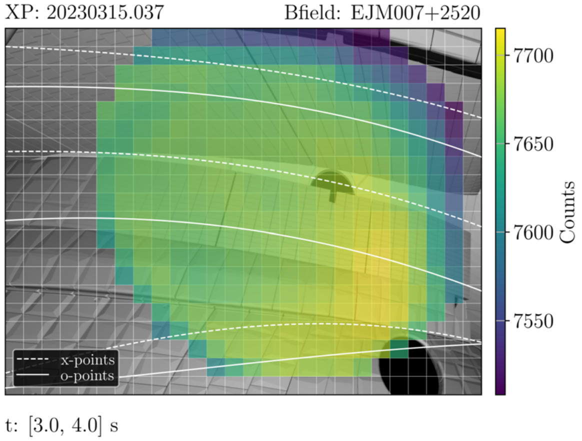

(b) Counts interpolated on foil

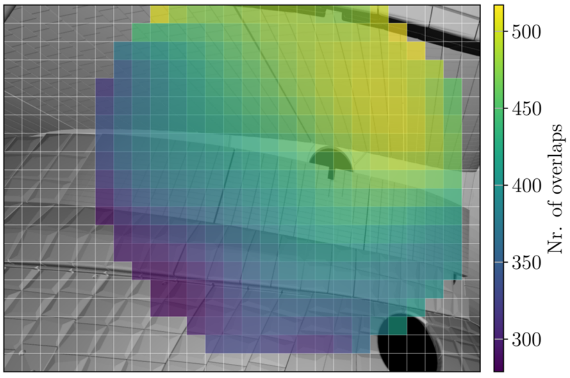

(c) Number of IR camera channel intersections

**FIG. 8.** (a) Image acquired by the IR camera during an example plasma discharge in units of raw counts, averaged in a one-second time interval. The useable area is highlighted with a white dashed line. Within this area a portion of the frame (red) and foil (blue) are visible. (b) Counts interpolated on the foil reference frame and binned on the 20 × 26 mesh of bolometer channels. (c) Number of IR camera channel intersections per bolometer channel.

Based on past studies addressing the spatial distribution of the calibration coefficients, a ±50% deviation across the foil surface is not considered to be uncommon.[18,43–46]

A spatially resolved calibration technique typically involves illuminating different points on the foil surface with a light source of known radiated power while measuring the evolution of the spatiotemporal temperature distribution with an IR camera.[47] More recently, lasers have been used for calibration experiments due to their well-defined collimation and power deposition profiles.[45,46] In situ calibration is also possible.[43,48,49]

In this paper, we employ a laboratory calibration setup as schematized in Fig. 9. The calibration measurements took place several months after the experimental campaign was concluded. In the meantime, the plasma-facing side of the 5 $\mu$m Au foil and frame was coated with a thin layer of Black 3.0 carbon spray using a handheld spray gun (unknown thickness). The coating was performed in 20 passes with ten-minute break times in between to allow drying of the layer to ensure good uniformity.[50] This is expected to increase the absorption coefficient (emissivity coefficient $\varepsilon$) of the foil and increase its thermal mass (reduce its sensitivity $S$) with respect to the operational foil. A uniform deposited layer of Black 3.0 is expected to affect only the magnitude of the calibration coefficients (and calculated $p_{abs}$) and not its distribution.

To recreate the W7-X experimental conditions mentioned in Sec. II, foil and frame are installed in a steel vacuum chamber and pumped down to $10^{-7}$ mbar. Both are held suspended by fitting nuts and washers on four steel rods passed through the four frame corner screw-holes (see Fig. 1). On the plasma-facing side of the foil (left-hand side), a $\lambda = 405$ nm 42 mW laser is mounted on an optical platform with a two-axis SIGMAKOKI steering mirror providing the 2D scanning motion.[49] This platform is inside a sealed aluminum safety box and screwed to a BK7 vacuum window, which is transparent to visible light (82% transmittance). A long 2 m optical path to the foil allows scanning of the full foil surface with minimal rotation of the mirror. On the opposite end (right-hand side), the temperature distribution on the foil backside is measured through an infrared-transmitting sapphire window using a high-resolution FLIR SC7650 camera. The counts are converted to $T$ using the

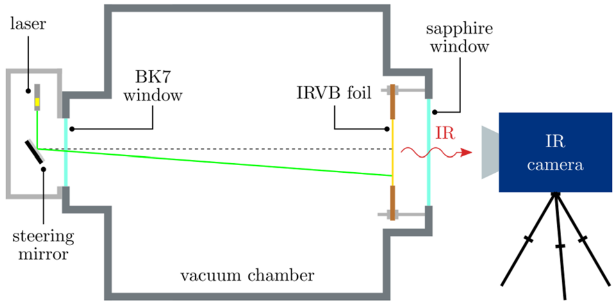

**FIG. 9.** Experimental setup for calibrating the foil thermal properties. With the foil and frame mounted inside a vacuum chamber, a visible laser is directed onto the foil using steering mirrors. The infrared emission from the foil backside is acquired with a high-resolution infrared camera.

coefficients discussed in Sec. IV. The foil and IR window are separated by a 15 cm distance perpendicular to the foil surface.

We measure the laser passing through the visible vacuum window using a SIGMAKOKI power meter.[49] This is performed to account for the finite (roughly 88%) window transmittance in the visible range (assuming negligible power absorption in air). We reduce the analysis to a Region Of Interest (ROI) centered around the laser spot [white box in Fig. 10(a)] of surface area $A_{ROI}$. The obtained power density reaching the foil is $p_{in} = \frac{34.5\text{ mW}}{A_{ROI}}$. The fraction of this power being absorbed by the foil is $p_{abs} = \varepsilon p_{in}$. We adjust the focal length of the laser to minimize the size of the heat spot on the foil. When a steel plate with a 1 mm screw-hole is placed on the optical path of the laser at an equal distance as the foil, >99 % of the laser power is transmitted through the aperture. This indicates a <1 mm FWHM of the laser power deposition profile at the foil surface. The resulting temperature distribution [see Fig. 10(a)] takes the shape of a Voigt curve centered on the laser spot.[46,49]

Particular care needs to be taken to avoid the Narcissus effect, i.e., the camera imaging the reflection of its own body or cold detector on the target.[15] Despite the camera vantage point being angled to avoid a frontal view, a self-reflection is still visible on the left-hand side of Fig. 10(a) (green). At the same time, the frame edges should remain visible in the calibration image, as they provide the spatial reference used to determine the IR camera channel size $l_{bol}$. In the temperature measurement, near the foil edge, it is still possible to notice the surface wrinkles shown in Fig. 1.

To extract the calibration coefficients, the spatial or temporal profile of the temperature increase resulting from laser irradiation is compared to synthetic data from the forward FD model[45] or fitted to an expected distribution.[46] If a spatially resolved calibration is performed, the same procedure has to be repeated for each location separately. In this article, we employ the calibration method recently developed by Federici in Ref. 51.

A single laser spot is applied to each calibration point until temperature saturation is achieved. 10 s of continuous static irradiation were found to be sufficient to reach thermal equilibrium for the case of our 5 $\mu$m-thick C-coated Au foil. Using a function generator, we pulse the laser power with a 10 s period square wave. Averaging the temperature inside the ROI produces the temporal evolution illustrated in Fig. 10(b). The characteristic thermal response of an absorber can be observed: a fast inverse exponential rise ($t$ = 2.5 s) followed by a flat-top ($t$ = 10.0–12.5 s). When the power is removed ($t$ = 12.5 s), the temperature drops following an exponential decay.

First, a value for $\varepsilon$ has to be defined, thus setting the blackbody component $p_{BB}$. Notably, this sets the temperature data $T$ as well, since the counts-to-temperature calibration requires the foil emissivity as an input. A lower (higher) set value for the surface emissivity means that a higher (lower) temperature is required to reach the same radiance, which determines the number of counts. To determine $\varepsilon$, we allow the foil to reach thermal equilibrium with its surroundings while measuring the ambient temperature with a thermocouple. Then, we scan over a range of emissivities and select the $\varepsilon$ value for which the difference between ambient temperature and temperature recorded by the camera is minimized. This is different from Ref. 51, as using our temperature calibration technique, a clear dependency of the solution on the foil emissivity could not be found.

Then, a background image averaged before the laser pulse [“background” in Fig. 10(b)] is subtracted from the temperature recording (in K units). The temperature $T_0$ averaged within this time interval and inside the ROI is used as the equilibrium temperature input for the FD method. Immediately after the laser pulse is initiated [“rise” in Fig. 10(b)], the temperature gradients are still small and the temperature rises. At this point, the thermal response of the IRVB foil is dominated by the time derivative component $p_{\dot{T}}$, while the Laplacian and blackbody components $p_{\nabla^2 T}$ and $p_{BB}$ can be neglected. Their relative contributions during the laser pulse can be better visualized in the noiseless forward FD calculation of Fig. 22(b). Likewise, at thermal equilibrium [“steady” in Fig. 10(b)], the time derivative of the temperature approaches zero.

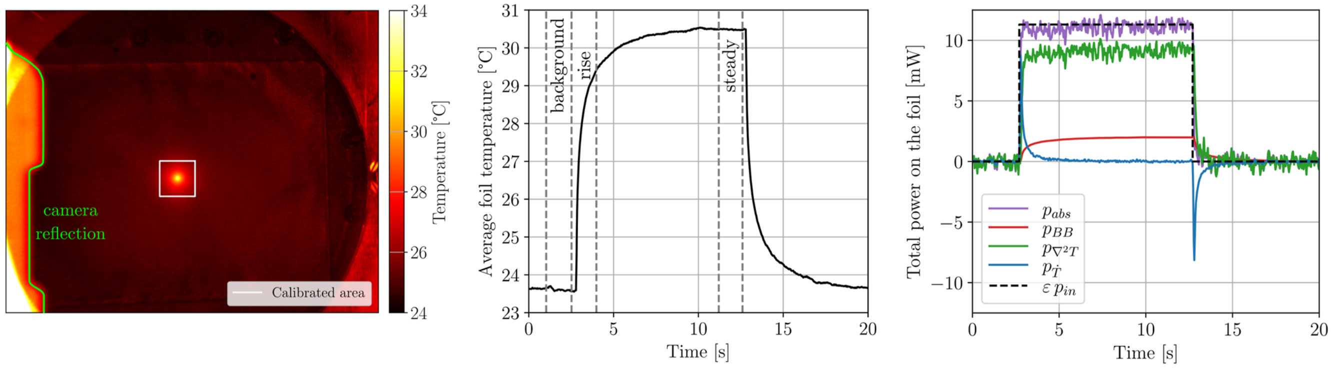

(a) Laser spot on the 5 $\mu$m Au foil (b) Temperature time trace (c) Calibration analysis

**FIG. 10.** (a) Temperature measured by the IR camera on the 5.0 $\mu$m C-coated Au foil during irradiation with blue 13.3 mW laser light. A white square surrounding the laser spot indicates the area examined in the calibration (3.3 × 3.3 mm$^2$). (b) Temperature rise on the 5.0 $\mu$m Au IRVB foil during irradiation with a blue 15.7 mW laser. The data are averaged in a 10 × 10 mm$^2$ square area around the laser spot. (c) Using the FD method, the heat transport coefficients can be calibrated from the foil response in the “rise” and “steady” time intervals. The calculation is based on separating and balancing the heat transport components (red, green, blue) to make the calculated power absorbed by the foil (purple) matches the applied laser power (black dashed line).

Rearranging Eq. (2),[51] it is possible to derive two independent estimates of the product $\kappa S$ from the "rise" portion [Eq. (3)] and of $S$ itself from the "steady" portion [Eq. (4)],

$$\kappa\, S = \frac{\sum p_{\dot{T}}}{p_{abs}}, \tag{3}$$

$$S = \frac{\sum p_{\nabla^2 T}}{p_{abs} - \sum p_{BB} + \sum p_{\dot{T}}}, \tag{4}$$

where $\sum p_{BB}$, $\sum p_{\dot{T}}$, and $\sum p_{\nabla^2 T}$ are the power density values calculated per IR camera channel and summed up inside the ROI. When using the calibrated coefficients $(\varepsilon, \kappa, S)$ to infer $p_{abs}$, we retrieve the exact amount of power specified in the input (plus random noise oscillations). The temporal profile, shown in purple in Fig. 10(c), follows the expected square wave behavior (plotted as a dashed black line).

A major advantage of this approach is that it does not rely on matching the experimental data with numerical simulations, which can be time-intensive and lead to a non-unique solution for a combination of $[\varepsilon, \kappa, S]$. Using the forward-calculated data with a NET of 10 mK, as detailed in Appendix B, the intrinsic uncertainty of this method in retrieving the calibration coefficients was estimated to be <5 % for a 5.0 $\mu$m Au foil-like thermal response.

After probing a dozen points on the foil surface with the laser, we calibrate each point separately. The three calibration coefficients averaged over all the sample points are as follows: $\varepsilon = (0.899 \pm 0.009)$, $\kappa = (6.7 \pm 0.8) \times 10^{-5}$ m$^2$ s$^{-1}$, $S = (320 \pm 42)$ KW$^{-1}$ (noted in Table I under the entry "OP2.1"). If the foil had homogeneous heat conductivity $k$ equal to the nominal gold value, this sensitivity would yield a thickness $t_f$ = 2.53 $\mu$m [Eq. (A11)]. This is about half the specified value of 5.0 $\mu$m.[15]

**TABLE I.** Useful parameters for the IRVB diagnostic at W7-X.

| Quantity | Units | OP2.1 | OP2.2 |
|---|---|---|---|
| $\sigma_{IR}$ | mK | 70 | 60 |
| $\sigma_{bol}$ | mK | 7 | 10 |
| $l_{IR}$ | mm | 0.16 | 0.28 |
| $l_{bol}$ | mm | 3.3 | 2.0 |
| $A_{IR}$ | mm$^2$ | 0.0256 | 0.0801 |
| $A_{bol}$ | mm$^2$ | 10.89 | 4.0 |
| $f_{IR}$ | Hz | 200 | 200 |
| $f_{bol}$ | Hz | 50 | 50 |
| $d_{pin}$ | mm | 5.0 | 5.0 |
| $A_{pin}$ | mm$^2$ | 25.0 | 25.0 |
| $N$ | ⋯ | 425 | 50 |
| $k$ (nom.) | Wm$^{-1}$ K$^{-1}$ | 318 | 72 |
| $\kappa$ (nom.) | $10^{-5}$ m$^2$ s$^{-1}$ | 12.7 | 2.34 |
| $\kappa$ (cal.) | $10^{-5}$ m$^2$ s$^{-1}$ | 6.7 | 1.1 |
| $S$ (nom.) | KW$^{-1}$ | 630 | 5500 |
| $S$ (cal.) | KW$^{-1}$ | 320 | 15 000 |
| $t_f$ (nom.) | $\mu$m | 5.0 | 2.5 |
| $t_f$ (cal.) | $\mu$m | 2.53 | 7.0 |
| $\varepsilon$ | ⋯ | 0.754 | 1.0 |
| $NEPD$ | Wm$^{-2}$ | 5.82 | 1.99 |

An optimal ROI size of 10 × 10 mm$^2$ was determined through tests on synthetic data, as explained in Appendix B (see Fig. 25 for example). This guarantees that all the laser power is being accounted for and that the thermal response can be accurately resolved while keeping a satisfactory SNR.[51] However, a smaller ROI of 3.3 × 3.3 mm$^2$ was defined in the experiments, as the optimized value was not available yet at the time. In addition, the counts-to-temperature conversion coefficients were calibrated for the diagnostic camera (FLIR SC8303) and might lead to inaccuracies when applied to a different camera model in the lab (FLIR SC7650). A new calibration employing the proper counts-to-temperature conversion, optimal ROI size, and extended scanning of the foil surface is planned for the future.

## VI. EXPERIMENTAL RESULTS

Here, we apply the post-processing procedure to experimental data acquired during the 2022–2023 experimental campaign (OP2.1). The temperature recorded on the foil reference frame can now be analyzed to extract the incident power information $p_{in}$. Doing this requires knowledge of the equilibrium temperature of the foil, $T_0$, which is estimated pre-discharge. We measure the frame temperature by averaging the counts within the region contoured with a red line in the IR camera image shown in Fig. 8(a) (assuming the same emissivity as the foil).

It can be noticed from Fig. 3 that the endoscope front is rather near the far-SOL and exposed to heat loads from the plasma as well as the heating systems. Given that the diagnostic is only inertially cooled, a considerable temperature rise of the endoscope front cap is expected. A lack of temperature measurements at the front plate prevents a direct quantification of this warm-up effect. Still, we can measure the evolution of the average foil temperature $\langle T \rangle$ throughout the day using the IR camera and track temperature drifts.

Outside of plasma discharges at thermal equilibrium, this value should settle to the temperature of the foil surroundings. Observations from the last experimental campaign reveal that the average foil temperature keeps rising until long after the discharge is terminated. This suggests a significant amount of residual heat flowing from the front to the back of the endoscope (see Fig. 11). The foil temperature rapidly increases during each discharge in response to the incoming power (spikes). After the heating systems are switched off, $\langle T \rangle$ quickly decays as the foil cools down. Often the foil temperature post-discharge does not equilibrate to its original pre-discharge value during the ~10 min interval in between shots. The consequence is a buildup of $\langle T \rangle$ during the day.

One consequence of this warm-up effect is the possibility of damage to the diagnostic. This is unlikely considering the expected thermal loads at the port (<100kWm$^{-2}$), the all-steel plasma-facing materials, and the large thermal mass of the IRVB endoscope. However, the diagnostic performance might be affected. For example, the varying thermal environment of the foil during the plasma discharge could influence the incident radiation power calculation. A drift of the equilibrium temperature of the foil relative to the initial (pre-discharge) value would be interpreted as an additional source of incident power mixed with the plasma radiation. In addition, a

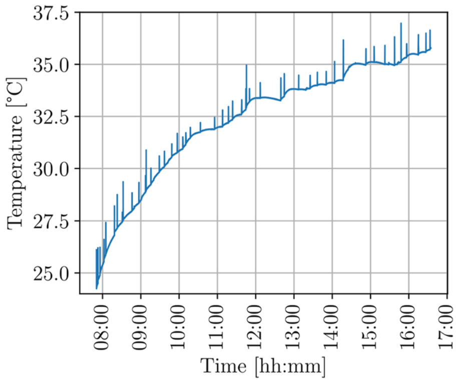

**FIG. 11.** Time evolution of the average foil temperature during a whole campaign day. Each temperature spike corresponds to a pronounced temperature increase due to a plasma discharge, while the slow increase is due to heat diffusion from the endoscope front.

non-uniform thermal environment of the foil complicates the analysis by introducing IR reflection features and a non-uniform cooling response of the foil. For these reasons, a redesign of the diagnostic to include active water cooling is underway. This will ensure better stability during long pulse operation.

### A. Inference of the incident radiation power

As an example, we analyze one hydrogen plasma discharge run in March 2023 in the standard magnetic field configuration: XP:20230315.037. The overview plot of Fig. 12 below reports the time trace of the most relevant plasma parameters for this analysis: input heating power $P_{heat} = 4$ MW, total radiated power $P_{rad} = 1.2$ MW (attached plasma, $f_{rad} = 0.3$), line-integrated density $\int n_e \, \mathrm{dl} = 8.0 \times 10^{19}$ m$^{-2}$, and diamagnetic energy $W_{dia} = 550$ kJ. All plasma parameters are fairly constant throughout the discharge until termination ($t = 10.0$ s). The only exception is an injection of tungsten impurities via Laser Blow-Off (LBO)[52] at $t = 5.0$ s, which perturbs both the plasma diamagnetic energy and the radiation signal.

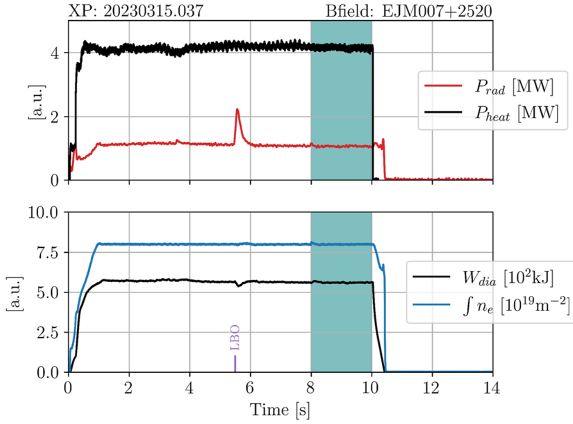

**FIG. 12.** Overview of plasma discharge XP:20230315.037 in two panels. Upper: Input heating power (black) and total radiated power (red). Lower: Line-integrated density (blue) and diamagnetic energy (black). Except for the startup phase ($t < 1.0$ s) and an LBO injection perturbing the plasma at $t = 5.0$ s, the discharge is otherwise steady-state.

First, the counts interpolated on the surface of the IRVB foil [see Fig. 8(b)] are converted to temperature units. The background temperature pattern is averaged over a 100 ms time interval pre-discharge and subtracted from the foil temperature data $T$. Noise fluctuations are reduced by binning the individual frames over a 20 ms window, downsampling the original frame rate of the camera $f_{IR} = 200$ Hz to $f_{bol} = 50$ Hz. Figure 13 reports the processed temperature data at thermal equilibrium. This is averaged over a 2.0 s time window from $t = 8.0$ s to $t = 10.0$ s (teal-shaded area in Fig. 12). Notably, some features can be distinguished in the temperature pattern, e.g., on the left-hand side inside the black dashed contour line. As the foil temperature distribution evolves during the discharge, these features are static and appear as points where the temperature values remain lower or higher than the surrounding areas. These probably arise due to bad interpolation accuracy from the IR camera view to the foil reference frame, especially near the edges of the imaged foil area.

The line-integrated power $p_{in}$ incident on each bolometer channel is evaluated by solving the 2D heat transfer equation.[10,15] This measured incident power is generally assumed to originate from radiative emission only. Other power loss components, such as those from neutrals, are considered to be of minor importance and are neglected in the analysis.[53] In this case, the incident power is the absorbed power value $p_{abs}$ given by Eq. (2) divided by the transmission factor $f$ from mesh to bolometer channel (see Fig. 14),

$$p_{in} = \frac{p_{abs}}{f} \qquad f = 0.53 \ \cos(\beta), \tag{5}$$

where 0.53 is the optical throughput of the microwave mesh. All the radiation power reaching the bolometer foil is assumed to be absorbed, meaning that the calculated value is not rescaled using the foil emissivity as performed for the laser calibration (Sec. V).

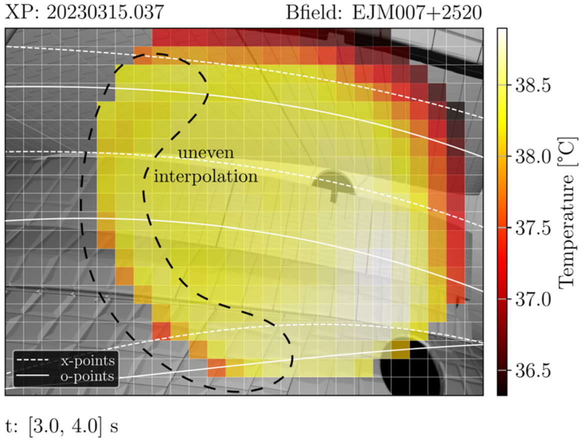

**FIG. 13.** Temperature distribution after interpolation on the bolometer channels. The data are averaged over a 0.5 s window in steady-state conditions to reduce noise ($t = 9.5$–$10.0$ s, teal-shaded area in Fig. 12).

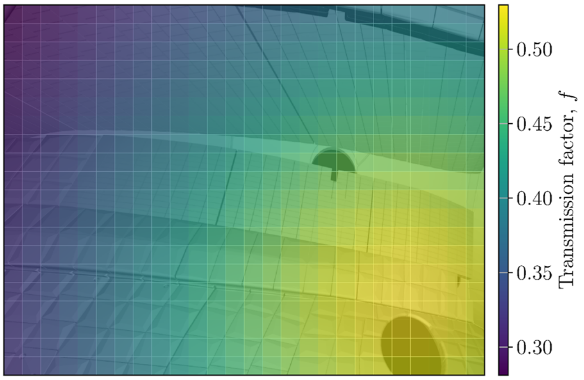

**FIG. 14.** Transmission factor between the microwave mesh and each bolometer channel. In the upper left corner of the foil, the incident power is cut by more than a factor of ×3.

Although the plasma radiated power is expected to be stationary throughout most of the discharge, a time-dependent behavior is observed. Similar features to those highlighted in Fig. 13 appear in the $p_{in}$ pattern and build up over time, as noticeable in the $p_{in}$ measurement of Fig. 15(a). They are currently interpreted as errors due to the static features present in the temperature data. In addition, non-uniformities in the thermal response of the foil could play a role (less likely given the observed temperature response in the lab experiments). This second contribution could be removed by using a spatially resolved map of calibration coefficients ($\varepsilon$, $\kappa$, $S$) on the foil. Another cause for the residual pattern could be the presence of a hot source near the foil (e.g., due to warm-up of the microwave mesh or baffles). However, this residual pattern is not observed in the upgraded OP2.2 design (discussed later in Sec. VI C), making the latter explanation unlikely.

Once the heating power is removed, the plasma rapidly collapses, quickly dissipating the stored energy. Part of this energy is dissipated in the form of radiation, usually in a 0.1–0.7 s time window after the heating power cutoff (see Fig. 12 at $t = 10.5$ s). No measurable amount of power is expected to reach the foil after this point. However, the observed buildup features persist in the IRVB power measurement and drop to zero following the time behavior of an exponential decay. We assess this residual signal $p_{res}$ by averaging the IRVB measurement in a 100 ms time window after plasma termination, obtaining the image reported in Fig. 15(b). Notably, the residual power pattern is composed of positive and negative power features whose total sum across the foil is close to zero. Positive (negative) values correspond to regions where the static temperature features are fixed at a higher (lower) value relative to what heat transport would allow given the surrounding foil temperature.

To evaluate $p_{res}$ at different times within the discharge, we track the evolution of the absolute value of $p_{in}$ summed over the whole foil, labeled as $\sum |p_{in}|$ in Fig. 15(c). After plasma termination, we fit the time trace of $\sum |p_{in}|$ after plasma termination using an exponential decay (green line). The fit window is $\Delta t = 100$ ms wide, starting from the time where the $p_{res}$ pattern is estimated (pink point). Based on the fit, the value of $p_{res}$ is traced back in time until the power cutoff (dashed gray line). Going further back in time $t$, this point is extrapolated to the beginning of the discharge using a logarithmic gain function (orange),

$$p_{res} = p_{res0} - \exp\left(-\frac{t}{\lambda}\right), \tag{6}$$

where $p_{res0}$ is the value of residual power extrapolated at the cutoff and $\lambda$ is the characteristic time constant obtained from fitting the exponential decay. By joining the two time traces (orange and green), we obtain a temporal profile for the expected $p_{res}$ evolution. We use this profile to rescale the $p_{res}$ pattern before subtracting it from $p_{in}$. The underlying assumption is that the $p_{res}$ contribution does not change in distribution but only in intensity during the discharge. At present, this method can be applied exclusively to discharges with constant input heating power. When $p_{in}$ is corrected in this way, the radiation pattern remains constant and equal to Fig. 16 throughout the discharge.

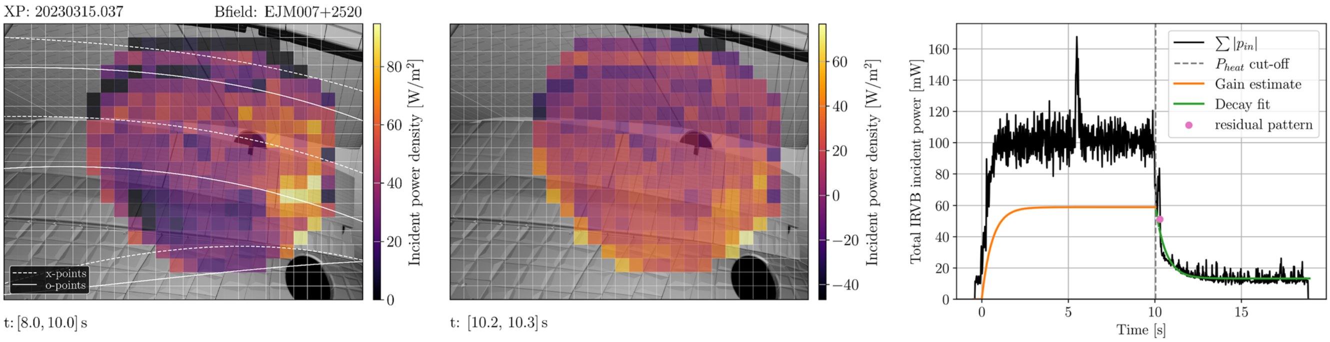

(a) Incident power $p_{in}$

(b) Residual pattern $p_{res}$

(c) Temporal plot of $\sum p_{in}$

**FIG. 15.** (a) Incident power signal $p_{in}$ inferred by solving the heat transport equation on the temperature data during the plasma discharge XP:20230315.037. (b) Residual power load component on the foil $p_{res}$, averaged in $t = 10.5$–$10.6$ s. (c) Temporal plot of the absolute value of $p_{in}$ summed up on the whole IRVB foil. The residual power load can be estimated after the heating power cutoff (pink point). Its time behavior can be fitted with an exponential decay (green) and estimated during the discharge with a matching inverse exponential gain (orange).

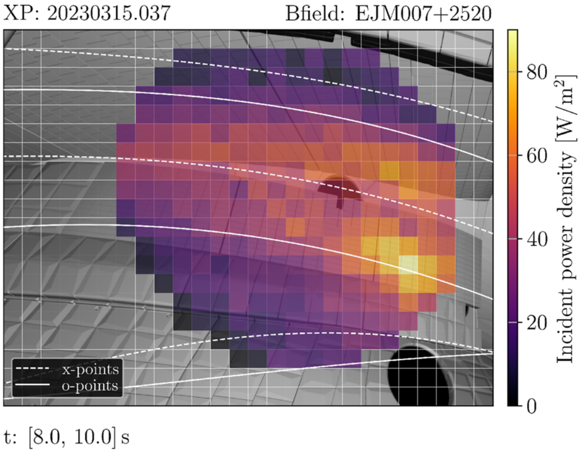

**FIG. 16.** Incident power signal measured during a plasma discharge corrected by subtracting $p_{res}$. Although the plasma conditions do not change, $p_{in}$ builds up over time and changes in distribution.

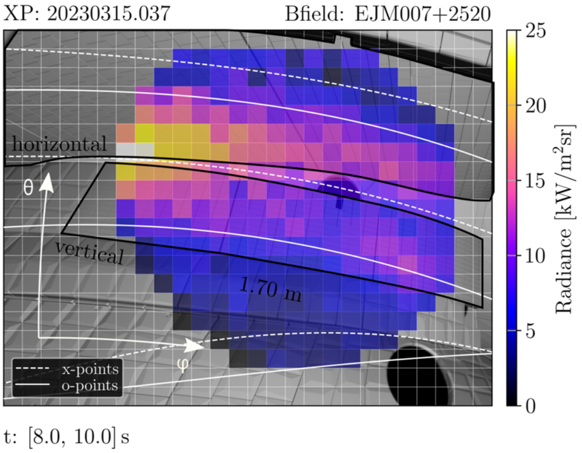

**FIG. 17.** IRVB measurement of the plasma radiance $L$ obtained by normalizing the line-integrated power by each bolometer channel geometry (the $p_{res}$ correction is included). Superimposed is a view of the machine CAD model and the traces of the island X-points (dashed lines) and O-points (solid lines) in standard magnetic field configuration, both projected on the foil view. Two white arrows identify the poloidal and toroidal directions $(\theta, \varphi)$. The vertical and horizontal divertor target plates are highlighted by a black contour line.

## B. Analysis of plasma radiation

We can now analyze the features of the corrected radiated power signal. Having removed the influence of $p_{res}$, this is a measurement of plasma radiation only. The Noise Equivalent Power Density (NEPD) on $p_{in}$ resulting from the analysis procedure can be calculated through[47,53]

$$NEPD = \frac{\mu_{noise}}{A_{bol}} = \frac{\sqrt{10}\,\sigma_{IR}}{S\sqrt{m\,N}}\sqrt{\frac{1}{A_{bol}^2} + \frac{f_{bol}^2}{5\,\kappa^2}}, \tag{7}$$

with $\sigma_{IR}$ camera NET, $m = f_{IR}/f_{bol}$ frame averaging, and $N = A_{bol}/A_{IR}$ number of IR camera channels per bolometer channel.[47] The IR camera NET measured at $T_0 = 28\,^\circ\mathrm{C}$ on a pre-discharge recording is typically $\sigma_{IR} = 70$ mK. All useful IRVB quantities are listed below in Table I "OP2.1." With these parameters, Eq. (7) yields $NEPD = 5.82\ \mathrm{Wm}^{-2}$, which corresponds to $SNR = 7$ for a typical incident power density level of 40 $\mathrm{Wm}^{-2}$ (e.g., the case presented in Sec. VI A).

As anticipated in Sec. IV, the varying throughput of the pinhole to each bolometer channel affects the power distribution on the foil surface. To remove the pinhole effect, the line-integrated power data can be normalized to the individual LoS geometry, as shown in Fig. 17. Namely, we divide the measured power by its etendue $e$ [see Eq. (1)] to obtain the measured radiance (or brightness) $L$ $[\mathrm{Wm}^{-2}\,\mathrm{sr}^{-1}]$

$$L = \frac{p_{in}\,l_{bol}^2}{e}. \tag{8}$$

Doing so reveals a radiance pattern mostly localized in a toroidally aligned band in the center of the IRVB view (toroidal and poloidal directions inside the IRVB view are indicated by white arrows). The core volume and far SOL appear darker, indicating a relatively lower emissivity in these regions. The distribution is characterized by two distinct radiation stripes, one per target plate (highlighted in black). This double-stripe distribution is reminiscent of the power load deposition pattern on the targets in standard configuration,[25,54] as will become more evident later in Sec. VI C [see Fig. 20(b) later]. Future work will delve into the correlation of the IRVB radiated power measurement with the strike line geometry at W7-X.

A projection of the island X- and O-point traces is overlaid on the plot to visualize the magnetic field geometry of the standard W7-X configuration (dashed and solid white lines, respectively). Using the vertical target plate as a spatial reference (highlighted by a black contour line), we can estimate the toroidal extent of the IRVB FoV on the far (inner wall) side to be ~1.90 m (1.20 m with the current partial foil coverage). This can help quantify the spatial gradients of plasma emissivity in the toroidal direction.[35]

$L$ can be further normalized to the LoS length $d_{LoS}$ crossing the plasma volume [Fig. 6(c)] and the total solid angle $4\pi$.[37,39] The result is the chord brightness measurement $\varepsilon_{chord}$ $[\mathrm{Wm}^{-3}]$ illustrated in Fig. 18,

$$\varepsilon_{chord} = \frac{4\pi}{d_{LoS}} L. \tag{9}$$

This quantity represents the plasma emissivity averaged within the bolometer LoS (see Ref. 37) and is therefore more representative of the actual plasma radiating structure. We find steep spatial gradients of the measured plasma emissivity across both the poloidal and the toroidal directions (white arrows). The overall scale of the divertor chord brightness signal is comparable to preliminary measurements from the resistive divertor bolometry system.[35]

In the poloidal direction $\theta$, a sharp separation takes place between the two radiation stripes and in the far SOL. Our signal originating from this region is mostly composed of random noise fluctuations. This noise component is enhanced when dividing by the intersection length $d_{LoS}$, which becomes vanishingly small in the

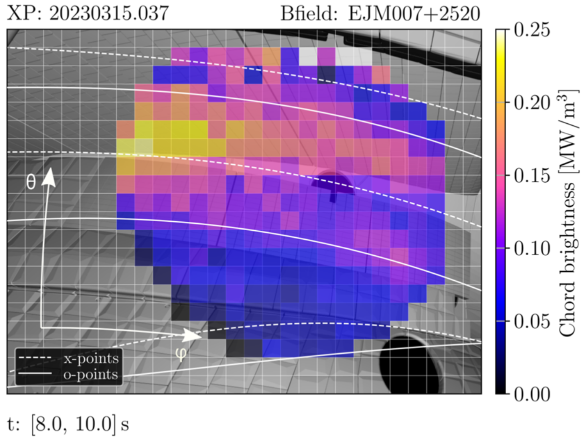

**FIG. 18.** IRVB measurement of the plasma chord brightness $\varepsilon_{chord}$ on the upper divertor unit. The data were acquired in standard magnetic field configuration, in attached regime, without impurity seeding.

top-right corner of the IRVB FoV. A considerable non-uniformity of the emissivity is also observed in the toroidal direction $\varphi$. The emissivity of the upper stripe feature, for example, varies by a factor of ×2 or more across the volume imaged by the IRVB. Mapping of the 2D poloidal radiation distribution reconstructed with tomography suggests that these radiation stripes originate near the surface of the divertor target plates.[35]

## C. Improved design

An upgraded design was developed for the new (OP2.2) experimental campaign, referred to as "OP2.2" in Table I. New Au-plated parabolic mirrors with an adjusted (152 mm) focal length are mounted to image the entire surface of the bolometer foil, as shown in Fig. 19(a). As a result, the available FoV of the diagnostic is extended to the full view introduced in Fig. 5. The camera coverage of the foil surface is also more uniform and centered, reducing optical distortions. In addition, a much larger area of the Cu frame is sampled. This simplifies the task of tracking temperature drifts as well as mechanical oscillations.

The 5.0 $\mu$m-thick absorber is substituted for a thinner 2.5 $\mu$m foil, improving the sensitivity of the temperature measurement (lower $t_f$, higher $S$). Moreover, the gold foil material is substituted for platinum, which favors steeper temperature gradients (lower $\kappa$) and, therefore, a higher spatial localization of the temperature features (see Fig. 23 in Appendix B). This allows the use of a finer grid of $33 \times 43 = 1419$ bolometer channels [black lines in Fig. 19(a)] for an improved spatial resolution of the IRVB diagnostic ($l_{bol} = 2$ mm). Like gold, the platinum material is readily available and can be rolled similarly to obtain thin metallic foils. Furthermore, gold is more prone to transmutation due to its larger neutron capture cross section. This makes platinum a more favorable material for a reactor-relevant diagnostic.[46,55]

Figure 19(b) reports a typical foil temperature measurement performed in OP2.2 during a standard configuration plasma discharge. The data are averaged in a time window at steady-state conditions with plasma parameters similar to those of the example discharge discussed in Sec. VI A: input heating power $P_{heat} = 4.0$ MW, total radiated power $P_{rad} = 0.9$ MW (attached plasma, $f_{rad} = 0.25$), line-integrated density $\int n_e \, \mathrm{dl} = 7.5 \times 10^{19}$ m$^{-2}$, and diamagnetic energy $W_{dia} = 550$ kJ. Thanks to the higher SNR and lower thermal diffusivity, the two-striped pattern associated with plasma radiation can already be distinguished in the $T$ distribution. Compared to Fig. 13, the image quality is greatly enhanced, and no bad interpolation features appear.

This benefits the quality of the absorbed power measurement as well, as shown in Fig. 19(c). With the new OP2.2 design, the divertor radiating structure is sampled with a wider collection angle and sharper definition. As a consequence, the radiation distribution measured by IRVB is more peaked with respect to the OP2.1 example of Fig. 16. No residual features are observed in $p_{in}$. Table I lists the

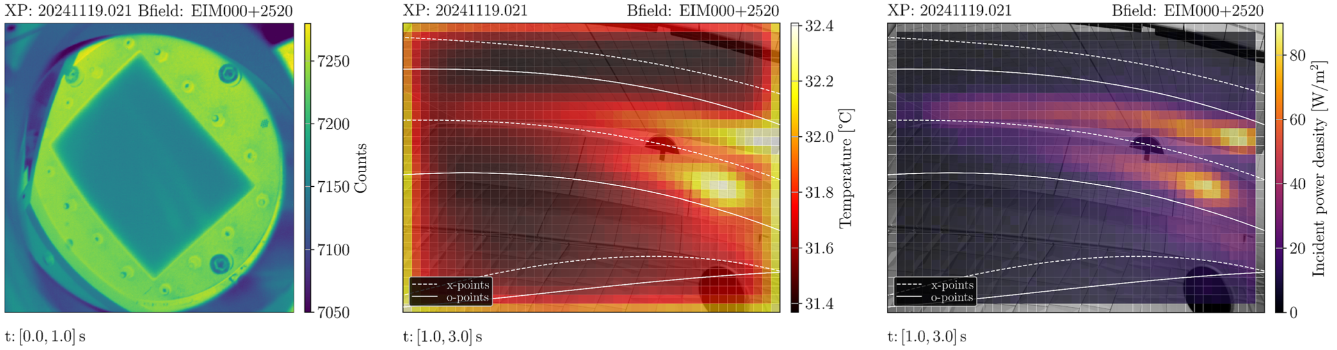

(a) OP2.2 IR camera view (b) OP2.2 $T$ measurement (c) OP2.2 $p_{in}$ measurement

**FIG. 19.** IRVB measurement of a standard configuration plasma experiment during the OP2.2 campaign: (a) IR camera image on the new 2.5 $\mu$m-thick Pt foil mediated by the new IR mirrors, (b) temperature data interpolated on the foil reference frame at thermal equilibrium, and (c) inferred absorbed power. A mesh of black lines is overlaid on the foil to show the new grid of bolometer channels after interpolation on the camera view [similar to Fig. 7(c)]. The data are averaged in a 2.00 s time window ($t$ = 1.0–3.0 s) in steady-state conditions.

calibration parameters, which are obtained following the same calibration procedure detailed in Sec. V. Their values averaged across 12 different points on the foil are $\varepsilon = 1.0$, $\kappa = (1.1 \pm 0.2) \times 10^{-5}\ \mathrm{m}^2\ \mathrm{s}^{-1}$, $S = (15\,000 \pm 5)\ \mathrm{KW}^{-1}$. Due to the smaller bolometer channel size, a smaller number $N = 50$ of IR camera channels are binned into each bolometer channel. In combination with the new thermal properties of the foil, this results in a noise level $NEPD = 1.99\ \mathrm{Wm}^{-2}$ for the OP2.2 design (SNR = 15).

Using Eqs. (8) and (9), we convert the absorbed power data to units of chord brightness, obtaining the measurement plotted in Fig. 20(a). This new emissivity measurement acquired in the OP2.2 campaign confirms the OP2.1 IRVB observations discussed in Sec. VI B and extends them to more regions of the plasma. The improved spatial resolution and SNR allow a more accurate comparison to the pattern of power load deposition on the divertor targets, shown in Fig. 20(b). In particular, the toroidal gradients of the plasma emissivity appear to match the toroidal distribution of the target power load. Here, the target heat flux is calculated by the W7-X wall thermography system[56] for the comparable discharge of Fig. 12 and averaged over the same time interval as the IRVB data (teal fill). The heat flux data are then projected on the IRVB FoV for better comparability with the measured IRVB emissivity.

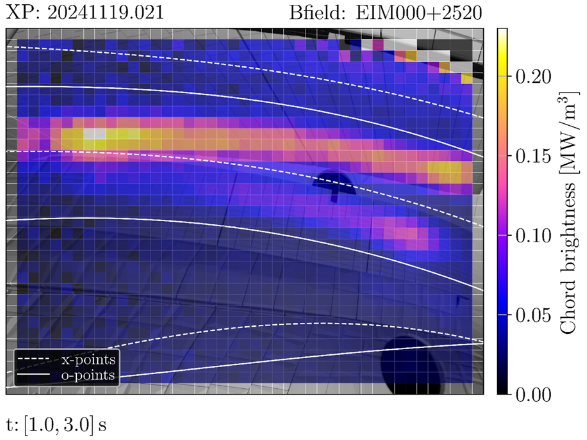

(a) Line-averaged emissivity (IRVB)

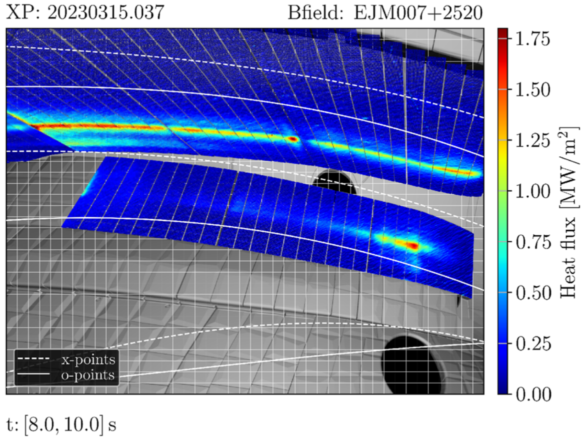

(b) Heat flux on targets (thermography)

**FIG. 20.** (a) Chord brightness measurement resulting from normalizing the incident power image of Fig. 19(c). (b) Power deposition pattern on the divertor targets calculated by the thermography system for the equivalent plasma discharge of Fig. 12. The heat flux data are mapped on the IRVB FoV.

Finally, we can quantify the spatial gradients of the plasma emissivity. Each LoS roughly covers a $5 \times 5\ \mathrm{cm}^2$ area on the vertical divertor target plates. Focusing our attention on the right-hand side of the lower radiation stripe, we can notice how the plasma emissivity drops by at least a factor ×2 in a span of 10 cm in the toroidal direction when moving toward the right-hand side end of the view (positive field direction). Proper characterization of the toroidal emissivity gradients is crucial for an accurate estimation of the total plasma radiated power (power exhaust) and for 3D tomography.[35,39]

These preliminary results showcase the potential of the IRVB concept as a diagnostic for radiated power measurements in a magnetic confinement plasma device. Its imaging capability is particularly beneficial to assess the three-dimensional distribution of plasma radiation in stellarator devices. Future plans at W7-X involve using the IRVB to characterize radiation asymmetries, track the radiation front movement, aid tomographic reconstructions, and improve the total $P_{rad}$ proxy.[57] A further upgrade of the IRVB diagnostic is foreseen for the next experimental campaign. This will include active water cooling and a larger bolometer foil that will provide an extended FoV.

## VII. CONCLUSIONS

The design of the IRVB diagnostic for W7-X was introduced, and its data analysis procedure was detailed from operating principles to data acquisition and post-processing of the signal. A set of laboratory experiments was conducted to calibrate the thermal properties of the 5 $\mu$-thick gold absorber foil by means of laser irradiation. Only 46% of the entire foil surface is imaged by the IR camera. Still, the available 239 bolometer channels provide a satisfactory imaging capability. The IRVB provided the first images of plasma radiated power in the W7-X island divertor during the OP2.1 campaign. IR radiation loads on the bolometer foil, likely caused by a warm-up of the microwave-blocking metallic mesh, were identified, and their contribution to the measurement was effectively subtracted for steady heating conditions. The IRVB measurements showed a divertor radiation pattern characterized by field-aligned stripes that are reminiscent of the strike line geometry. An upgraded design mounting a 2.5 $\mu$-thick platinum foil and adjusted IR mirrors showed greatly improved spatial resolution, uniformity, and sensitivity. The new setup with 1419 bolometer channels can better resolve the SOL radiating structure in the island divertor. Significant spatial gradients of the emissivity in the toroidal and poloidal directions were measured near the strike line location (order of factor ×2 per 10 cm displacement). Further upgrades of the IRVB diagnostic are foreseen for the next experimental campaign.

## ACKNOWLEDGMENTS

This work has been carried out within the framework of the EUROfusion Consortium, funded by the European Union via the Euratom Research and Training Program (Grant Agreement No. 101052200 — EUROfusion). The views and opinions expressed are, however, those of the author(s) only and do not necessarily reflect those of the European Union or the European Commission. Neither the European Union nor the European Commission can be held responsible for them.

This work was supported by the U.S. Department of Energy at Los Alamos National Laboratory, operated by Triad National Security LLC for the National Nuclear Security Administration (Contract No. 89233218CNA000001).

This research was supported by the NINS-DAAD International Personal Exchange Program, JSPS Grant No. 22KK0039, NIFS Grant No. SIU004 and, for B. J. Peterson, the Alfried Krupp Wissenschaftskolleg Greifswald underwritten by the Stiftung Alfried Krupp Kolleg and the Alfried Krupp von Bohlen und Halbach-Stiftung.

This work was supported by the U.S. Department of Energy, Office of Fusion Energy Sciences, under the Spherical Tokamak program, Contract No. DE-AC05-00OR22725.

## AUTHOR DECLARATIONS

### Conflict of Interest

The authors have no conflicts to disclose.

### Author Contributions

**G. Partesotti**: Data curation (lead); Formal analysis (lead); Investigation (equal); Methodology (equal); Validation (lead); Visualization (lead); Writing – original draft (lead); Writing – review & editing (lead). **G. A. Wurden**: Conceptualization (equal); Funding acquisition (equal); Investigation (equal); Resources (equal); Supervision (supporting); Writing – review & editing (equal). **F. Reimold**: Conceptualization (equal); Funding acquisition (equal); Investigation (equal); Project administration (equal); Resources (equal); Supervision (lead); Writing – review & editing (equal). **B. J. Peterson**: Conceptualization (equal); Investigation (supporting); Methodology (equal); Resources (supporting); Supervision (supporting). **F. Federici**: Conceptualization (supporting); Methodology (equal); Resources (supporting); Writing – review & editing (equal). **K. Mukai**: Conceptualization (supporting); Methodology (supporting); Resources (supporting); Supervision (supporting). **K. A. Siever**: Data curation (supporting); Formal analysis (supporting); Investigation (supporting). **J. von Miller**: Conceptualization (supporting); Data curation (supporting); Visualization (supporting). **D. Zhang**: Investigation (supporting); Writing – review & editing (supporting). **A. Demby**: Data curation (supporting); Investigation (supporting).

## DATA AVAILABILITY

The data that support the findings of this study are available from the corresponding author upon reasonable request.

## APPENDIX A: 2D HEAT TRANSFER EQUATION

In the high vacuum environment of the cryostat, heat convection and conduction with air are suppressed. Since the heat transfer perpendicular to the foil surface is much faster than that across the surface, the heat transfer solution can be treated as a 2D problem.[10] As a consequence, energy can be transferred into and out of a pixel only through radiative cooling or thermal contact with the neighboring pixels. To satisfy energy conservation, the temperature change $\Delta T$ of one pixel after a time interval $\Delta t$ must be due to three power components: heat diffusion to/from neighboring pixels $p_{\nabla^2 T}$, absorbed incident power $p_{abs}$, and blackbody (thermal) emission from the foil $p_{BB}$ (see Fig. 21). These are calculated in units of power per surface area on the foil. Notably, the quantity of interest here is $p_{abs}$ [$\mathrm{Wm^{-2}}$], or more specifically the absorbed fraction of the radiation power (per unit area) impinging on the foil. Each contribution will be expressed as a temperature change, here named $\Delta T_{\nabla^2 T}$, $\Delta T_{abs}$, and $\Delta T_{BB}$, respectively.

Starting with heat diffusion, the temperature change over time due to power diffusing on the foil surface is described by the two-dimensional equation for diffusion in the $x$ and $y$ directions

$$\frac{\partial T}{\partial t} = \kappa \left[ \frac{\partial^2 T}{\partial x^2} + \frac{\partial^2 T}{\partial y^2} \right], \tag{A1}$$

with $\kappa$ [$\mathrm{m^2\ s^{-1}}$] thermal diffusivity constant of the foil material.

When the foil is divided into pixels of dimensions $dx \times dy$, the diameter of the pixel should be chosen such that the thermal diffusion time of the pixel is larger than the frame interval $\Delta t$.[10] Using a simplified isotropic case $dx = dy = l_{bol}$, the pixel area is generalized as $l_{bol}^2 = dx\, dy$.

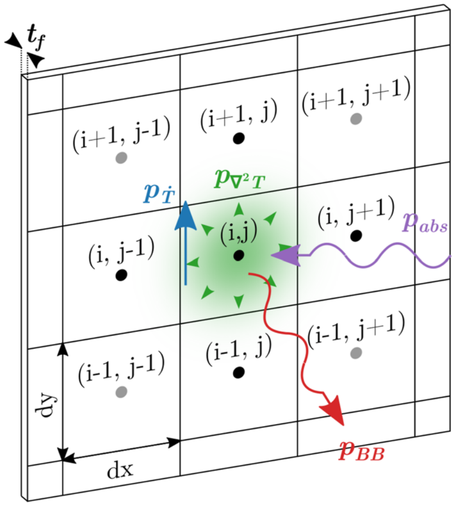

**FIG. 21.** Illustration of the bolometer foil grid and the power components that play a role in the 2D heat transfer calculation: absorbed (purple), diffused (green), radiated (red), and thermal (blue). Using the five-point stencil, diffusion is calculated only on adjacent pixels (darker-shaded points). When a nine-point stencil is used, diagonal diffusion (to the lighter-shaded points) is taken into account.

The 2D heat diffusion component can be discretized by approximating the Laplacian with a 5-point stencil. If $T(x, y)$ is the temperature of the foil at horizontal position $x$ and vertical position $y$ at a given time, the temperature change due to heat diffusion in/out of the pixel after time step $\Delta t$ is

$$\begin{aligned} \Delta T_{\nabla^2 T} &\simeq \kappa\left[\frac{T(x+dx,y)+T(x-dx,y)-2T(x,y)}{dx^2}\right]\Delta t \\ &+\kappa\left[\frac{T(x,y+dy)+T(x,y-dy)-2T(x,y)}{dy^2}\right]\Delta t. \end{aligned} \tag{A2}$$

In an isotropic case we can calculate the Laplacian term with

$$\nabla^2 T = L_{5p} * T(x,y), \tag{A3}$$

having represented the five-point stencil with the convolution kernel $L_{5p}$,

$$L_{5p} = \begin{bmatrix} 0 & 1 & 0 \\ 1 & -4 & 1 \\ 0 & 1 & 0 \end{bmatrix}. \tag{A4}$$

A nine-point stencil can be applied to more accurately model diffusion in the diagonal direction by using the kernel $L_{9p}$ (only applicable if $dx = dy$),

$$L_{9p} = \begin{bmatrix} 1/4 & 2/4 & 1/4 \\ 2/4 & -12/4 & 2/4 \\ 1/4 & 2/4 & 1/4 \end{bmatrix}. \tag{A5}$$

Regarding power absorption, the corresponding temperature change $\Delta T_{abs}$ can be written as the total absorbed energy $p_{abs}$ integrated over the pixel surface area $l_{bol}^2$ and time $\Delta t$ divided by the heat capacity of one pixel $C$ [JK$^{-1}$],

$$\Delta T_{abs} = \frac{p_{abs}\ l_{bol}^2\ \Delta t}{C}. \tag{A6}$$

The power lost by the foil through thermal radiation $p_{BB}$ is given by the Stefan–Boltzmann law

$$p_{BB} = -2\ \varepsilon\ \sigma_{SB}\ (T^4 - T_0^4), \tag{A7}$$

when $\varepsilon$ is the pixel emissivity, $\sigma_{SB}$ [Wm$^{-2}$ K$^{-4}$] is the Stefan–Boltzmann constant, and $T_0$ is the ambient (equilibrium) temperature. Here, the factor 2 takes into account emission from both sides of the bolometer foil absorber. An isotropic ambient temperature $T_0$ is assumed. This yields

$$\Delta T_{BB} = -\frac{2\ \varepsilon\ \sigma_{SB}\ (T^4 - T_0^4)\ l_{bol}^2}{C}\Delta t. \tag{A8}$$

We can rewrite the heat capacity as the specific heat capacity of the material $c$ [JK$^{-1}$ Kg$^{-1}$] times pixel mass, where the mass is just mass density $\rho$ times pixel area $l_{bol}^2$ times foil thickness $t_f$ (assuming uniform thickness),

$$C = l_{bol}^2\ t_f\ \rho\ c. \tag{A9}$$

At the same time, the thermal diffusivity $\kappa$ is defined as the ratio between the heat conductivity $k$ [Wm$^{-1}$ K$^{-1}$] and the product of density times specific heat, which allows us to express $C$ as

$$C = \frac{l_{bol}^2}{\kappa\ S}, \tag{A10}$$

where we defined the foil sensitivity $S$ [KW$^{-1}$] as

$$S = \frac{1}{k\ t_f}. \tag{A11}$$

Now we can write the set of equations that dictate the temperature change inside one pixel depending on the power influx or outflux

$$\begin{aligned} \Delta T &= \Delta T_{\nabla^2 T} + \Delta T_{BB} + \Delta T_{abs}, \\ \Delta T_{\nabla^2 T} &= \kappa\ \nabla^2 T\ \Delta t, \\ \Delta T_{BB} &= -2\ \kappa\ S\ \varepsilon\ \sigma_{SB}\ \left(T^4 - T_0^4\right)\ \Delta t, \\ \Delta T_{abs} &= \kappa\ S\ p_{abs}\ \Delta t. \end{aligned} \tag{A12}$$

If the incident power $p_{abs}$ is known, solving the 2D heat transfer equation [Eq. (A12)] for a given time step $\Delta t$ allows for a time-resolved forward model of the temperature distribution on the foil.

Experimentally, the 2D heat transfer equation is applied backward: the $p_{abs}$ information is extracted from a time-resolved video of the temperature distribution $T$ on the foil. Using Eqs. (A3), (A6), and (A8), we can rewrite Eq. (A12) in terms of the power. This way we obtain the backward 2D heat transfer equation, which provides a solution for the incident power by separating the different power components,[10,15]

$$\begin{aligned} p_{abs} &= p_{\nabla^2 T} + p_{BB} + p_{\dot{T}}, \\ p_{\nabla^2 T} &= -\frac{1}{S}\ \nabla^2 T, \\ p_{BB} &= 2\ \varepsilon\ \sigma_{SB}\ \left(T^4 - T_0^4\right), \\ p_{\dot{T}} &= \frac{1}{\kappa\ S}\ \frac{\mathrm{d}T}{\mathrm{d}t}, \end{aligned} \tag{A13}$$

where $p_{\dot{T}}$ is the variation in the thermal energy component. Hence, three major properties define the thermal response of the foil: $\varepsilon$, $\kappa$, and $S$.

## APPENDIX B: THE FINITE DIFFERENCE (FD) METHOD

In the following, we detail the Finite Difference (FD) method,[10] a numerical solution to the equations that model 2D heat transport on the foil surface. This approach can be applied in a forward fashion to simulate the temperature distribution $T$ for a known absorbed power distribution $p_{abs}$ [Eq. (A12)] or, conversely, in a backward fashion to infer the absorbed power from the temperature data [Eq. (2)]. Both variants require prior knowledge of the thermal properties of the foil in the form of three (calibration) coefficients: emissivity $\varepsilon$, thermal diffusivity $\kappa$ [m$^2$ s$^{-1}$], and sensitivity $S$ [KW$^{-1}$].

A FD method involves discretizing the problem both in space with pixel size $l_{bol}$ and in time with time step $\Delta t$. In the experiment, the former is limited by the available SNR (averaging over a larger pixel reduces the noise level $\sigma_{bol}$), and the latter is limited by the frame rate $f_{IR}$. In a synthetic case, the resolution choice is regulated by a trade-off between accuracy and computational cost. For numerical stability, the time step duration should be shorter than the characteristic time of thermal diffusion, which is proportional to $\frac{l_{bol}^2}{\kappa}$.[10] At each point in time, the three heat transport contributions are computed for each pixel depending on the input power (forward) or temperature (backward).

Figure 22(a) shows an example Gaussian power deposition pattern $p_{in}$ (0.2 mm standard deviation) resembling the irradiation point of a laser. This is applied to a 30 × 30 mm$^2$ foil surface subdivided into 150 × 150 pixels ($l_{bol}$ = 0.2 mm). The total sum of the input power is 35 mW.

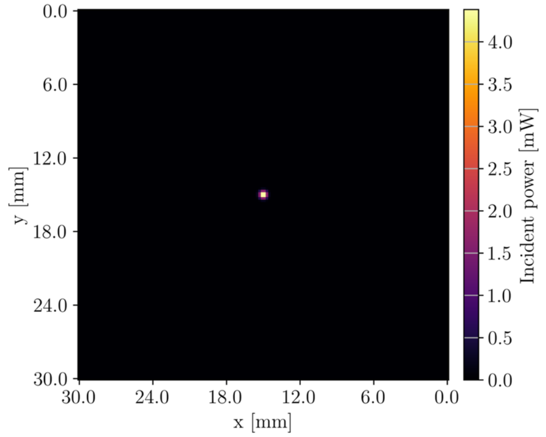

(a) Applied power, $p_{in}$

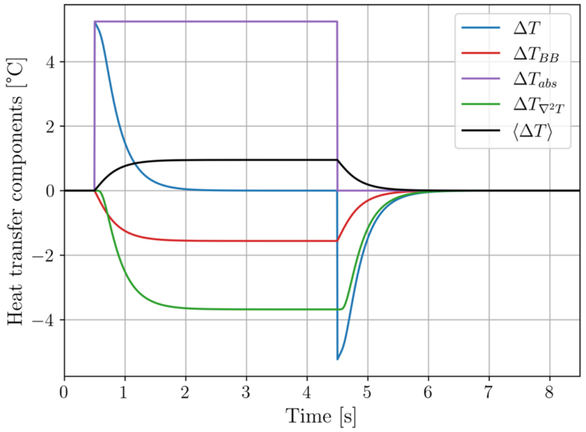

(b) Forward model components

**FIG. 22.** (a) Power deposition pattern applied to the IRVB foil and (b) temperature contribution of each component in the noiseless heat transport forward model, summed up on the whole foil: thermal radiation (red), absorbed power (purple), and heat diffusion (green). Their sum yields the temperature change on the IRVB foil (blue). The maximum temperature on the foil (black) saturates after a few seconds of power absorption (applied from $t$ = 0.5 s to $t$ = 4.5 s). The spatial and temporal resolution of this forward model is five times higher than typical experimental values.

In general, applied (incident) power $p_{in}$ and absorbed power follow the relation

$$p_{abs} = \varepsilon \, p_{in}. \tag{B1}$$

With the foil initially in thermal equilibrium at a uniform ambient temperature $T_0$ = 25 °C, the power phantom is applied as a square wave pulse of 4 s duration. At the boundary, the last row of pixels is assumed to be in thermal contact with an infinite reservoir at fixed temperature $T_0$, which mimics the heat sink action of the copper frame. Then, the thermal response of the foil is computed step by step with a time step $\Delta t$ = 0.1 ms and downsampled to $\Delta t$ = 5 ms ($f_{IR}$ = 200 Hz). This yields the same spatiotemporal resolution as the IR camera. Power deposition is preceded by 0.5 s of background and followed by 2 s of re-thermalization time to reconstruct the cooling process. With this spatiotemporal resolution, the simulation runtime is on the order of one minute on a local machine [virtual machine without parallel computing, central processing unit (CPU): AMD EPYC 9124 16-Core, graphics processing unit (GPU): NVIDIA A40-1B, RAM: 64 GB].

The individual heat transport components that contribute to temperature change $\Delta T$ are broken up in Fig. 22(b), summed over all foil pixels, and plotted vs time. These were estimated using Eq. (A12). Most notably, the thermal radiation (red) and diffusive (green) components are negligible at the absorbed power (purple) onset, when the temperature change (blue) peaks. At the end of the heating, $\Delta T$ switches from zero (thermal equilibrium) to negative, indicating that the foil is cooling down. The time trace of the maximum temperature on the foil is also plotted as a black solid line. Note that the maximum temperature value not only depends on the thermal characteristics of the foil but also on the power density of the applied power and the spatial resolution of the model. Applying the same laser power with a narrower (wider) focus or using a finer (coarser) calculation grid would result in a higher (lower) $\Delta T_{\max}$.

For this example, the thermal properties of the absorber are set to those of a pure gold foil ($k$ = 318 Wm$^{-1}$ K$^{-1}$, $\kappa$ = 12.7 × 10$^{-5}$ m$^2$ s$^{-1}$ as in Table I "OP2.1") of thickness $t_f$ = 5.0 $\mu$m with surface emissivity $\varepsilon$ = 0.75. The resulting sensitivity is $S$ = 630 KW$^{-1}$. A snapshot of the temperature distribution $T$ at $t$ = 4.0 s is reported in Fig. 23(a).

It can be noticed how the incident power features are blurred out in the temperature image as a result of the heat transport. In particular, materials with lower heat diffusivity $\kappa$ will present steeper spatial gradients and a slower time response, while materials with a higher $S$ factor will exhibit a higher temperature rise. To demonstrate this, the same simulation is repeated on a pure platinum foil ($k$ = 72 Wm$^{-1}$ K$^{-1}$, $\kappa$ = 2.3 × 10$^{-5}$ m$^2$ s$^{-1}$) of 2.5 $\mu$m thickness ($S$ = 5500 KW$^{-1}$) and emissivity $\varepsilon$ = 0.9. From the resulting temperature distribution reported in Fig. 23(b), two conclusions can be drawn: at the same applied power, the thinner Pt foil offers a more marked temperature rise ($\Delta T_{\max}$ = 17.5 °C) compared to the thicker gold ($\Delta T_{\max}$ = 3.5 °C), and higher localization of the temperature features (i.e., better definition). These qualities make the 2.5 $\mu$m Pt absorber a more favorable candidate for the IRVB detector.

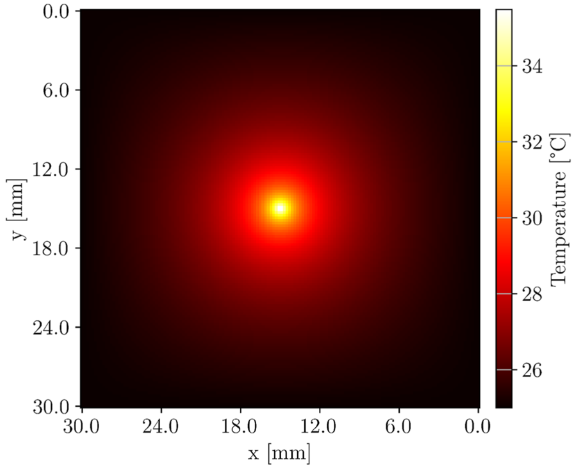

(a) Saturated $T$ pattern on 5.0 $\mu$m Au foil

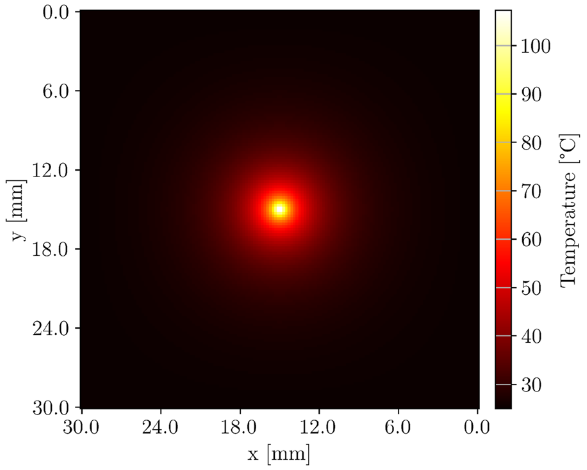

(b) Saturated $T$ pattern on 2.5 $\mu$m Pt foil

**FIG. 23.** Temperature distribution on the foil at thermal equilibrium (after $t$ = 4.0 s) for the cases of (a) 5.0 $\mu$m Au and (b) 2.5 $\mu$m Pt.

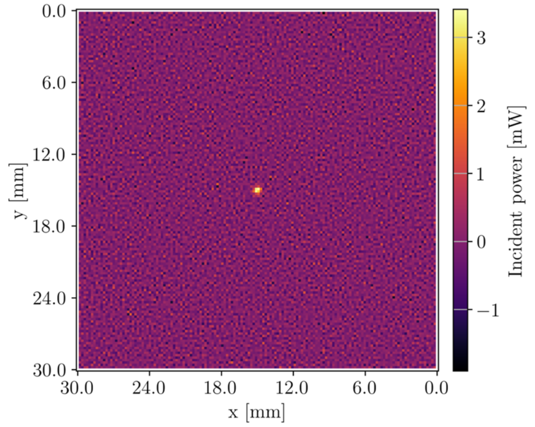

(a) Back-calculated power $p_{in}$

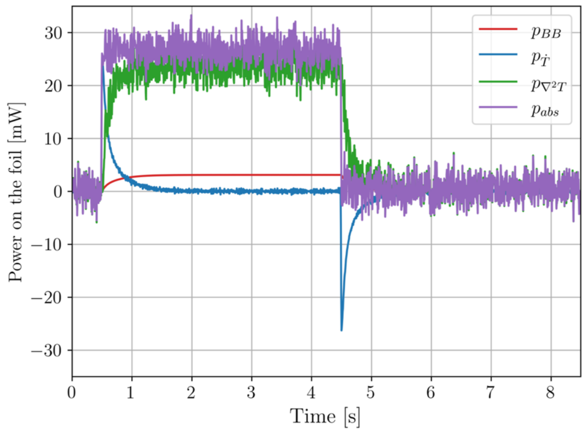

(b) Backward model components

**FIG. 24.** (a) Incident power on the IRVB foil back-calculated from the simulated temperature distribution, and (b) its heat components separated in a time trace plot. The color coding is the same as in Fig. 22. A random noise component of $\sigma_{bol}$ = 10 mK was introduced into the synthetic temperature data.

Finally, the calculated temperature video can be fed into Eq. (2) to test the backward FD solution, which is employed in the experiment to infer the absorbed power. Solving for the power requires knowledge of the equilibrium temperature $T_0$ of the foil surroundings, which in the experiment is typically estimated by measuring the frame temperature. To mimic the experimental NET, random noise fluctuations at $\sigma_{IR}$ = 70 mK are artificially included in the temperature data. Since the thermal contact with the frame is not known, heat transport at the boundary is modeled as fixed to the frame temperature (as in the ideal case). For this reason, as noticeable from Fig. 24(a), the very last row of pixels in direct contact with the edge is discarded from the power solution.

Taking advantage of the fact that the data are synthetic, we can compare the back-calculated $p_{abs}$ shown in Fig. 24(a) with the original applied power pattern of Fig. 22(a). As visible in Fig. 24(a), although the addition of a random noise component introduces background noise, the incident power features are conserved [compare to Fig. 22(a)]. Furthermore, negative values can appear in the solution, especially in areas of low incident power where the fluctuations can lower the temperature to below the assumed ambient value of $T = 25\,^{\circ}$C.

As per Figs. 22(b) and 24(b), the reports separate power components in the backward calculation. In this case, most of the noise in the absorbed power signal $p_{abs}$ (purple) is introduced by the diffusion component (green), while the time derivative (blue) and thermal radiation (red) components are largely unaffected.

Importantly, this synthetic analysis can be employed to validate the calibration procedure detailed in Sec. V. For example, different sizes of the ROI defined around the laser spot affect the accuracy of the calibrated coefficients. Figure 25 demonstrates this by comparing several calibration attempts of $\kappa$ (blue) and $S$ (red) on the

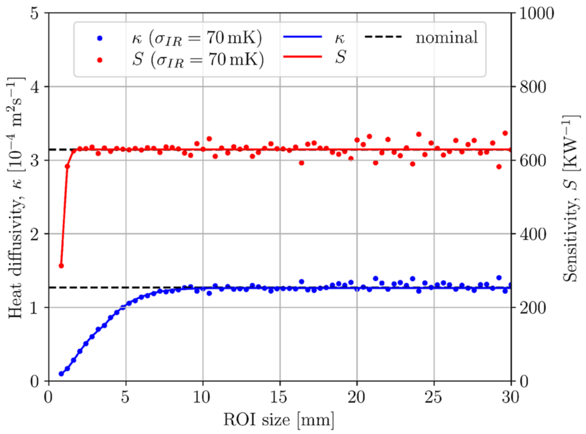

**FIG. 25.** Calibrated foil thermal properties $S$ (red) and $\kappa$ (blue) as a function of the size of the defined ROI. The calibration procedure is applied to the simulated thermal response of a 5.0 $\mu$m Au foil with (scatter points) and without (solid line) a 70 mK random noise level. A dashed black line indicates the nominal value.

synthetic data when selecting different areas around the power deposition spot for a case with noise (scatter points) and without noise (solid lines). On a fundamental level, the laser power needs to be entirely sampled by the ROI to be able to apply Eqs. (3) and (4). This is why the estimated $S$ rapidly diverges from the nominal one (black dashed line) for an ROI size smaller than 2 mm. A larger ROI improves the accuracy by including more data points but also lowers the SNR. However, a minimum size of at least $10 \times 10$ mm$^2$ is required to assess the foil diffusivity properly.

When the ROI size is >10 mm and no noise is applied, the calibration is exact and limited only by the numerical error (the relative deviation between original and calibrated coefficients is <0.01 %). With added noise, the deviation between input power to the forward model and output power from the backward model is 3% for the 5.0 $\mu$m Au case. In the 2.5 $\mu$m Pt case, the higher temperature response of the foil improves the SNR, lowering the relative error due to noise to 1%. The lower diffusivity also facilitates the estimation of the $\kappa S$ constant from the peak of the time derivative component [see Eq. (3)], allowing for a smaller ROI size of $5 \times 5$ mm$^2$.

Experimentally, the noise level in the inferred power can be reduced by binning adjacent pixels, by averaging frames together, or by increasing the number of time points over which the temporal derivative of the temperature ($p_{\dot{T}}$) is computed. This smoothing of the temperature data results in a lower spatial and temporal resolution of the final absorbed power measurement. Unlike the experiment, the synthetic calibration tests yield a strong and well-defined signal. For this reason, no binning was applied to the synthetic data, and a minimum of two consecutive points was used for the derivative calculation.

Although the incident power solution provided by the FD method is unique, its accuracy is still affected by the thermal properties of the absorber. A bolometer foil with low sensitivity and a slow time response will reduce the precision with which the time derivative power component is estimated, ultimately limiting the temporal resolution of the diagnostic. Likewise, broad spatial gradients on the foil caused by a significant parallel heat diffusion component prevent an exact unfolding of the incident power distribution, limiting the spatial resolution. Steady-state long-pulse operation at W7-X is beneficial in this regard, as the IRVB measurement can be averaged over a wide time interval to mitigate noise fluctuations. This, however, still prevents capturing quick radiation events (e.g., radiation collapse, fast transitions to detachment, impurity injections, etc.) for which good (i.e., at least 100 ms) time resolution is required.

## REFERENCES

[1] O. Schmitz, Y. Feng, M. Jakubowski, R. König, M. Krychowiak, M. Otte, F. Reimold, T. Barbui, C. Biedermann, S. A. Bozhenkov *et al.*, "Stable heat and particle flux detachment with efficient particle exhaust in the island divertor of Wendelstein 7-X," Nucl. Fusion **61**(1), 016026 (2020).

[2] R. A. Pitts, X. Bonnin, F. Escourbiac, H. Frerichs, J. P. Gunn, T. Hirai, A. S. Kukushkin, E. Kaveeva, M. A. Miller, D. Moulton *et al.*, "Physics basis for the first ITER tungsten divertor," Nucl. Mater. Energy **20**, 100696 (2019).

[3] R. Sano, B. J. Peterson, M. Teranishi, N. Iwama, M. Kobayashi, K. Mukai, and S. N. Pandya, "Three-dimensional tomographic imaging for dynamic radiation behavior study using infrared imaging video bolometers in large helical device plasma," Rev. Sci. Instrum. **87**(5), 053502 (2016).

[4] K. Mukai, G. Kawamura, S. Masuzaki, Y. Hayashi, H. Tanaka, B. J. Peterson, T. Oishi, C. Suzuki, M. Kobayashi, and K. Munechika, "Three-dimensional structure of radiative cooling in impurity seeded plasmas in the Large Helical Device," Nucl. Mater. Energy **33**, 101294 (2022).

[5] H. Meister, M. Bernert, W. Biel, M. Han, L. C. Ingesson, K. Mukai, F. Penzel, B. J. Peterson, R. Reichle, M. L. Reinke *et al.*, "Bolometer developments in diagnostics for magnetic confinement fusion," J. Instrum. **14**(10), C10004 (2019).

[6] L. Giannone, D. Queen, F. Hellman, and J. C. Fuchs, "Prototype of a radiation hard resistive bolometer for ITER," Plasma Phys. Controlled Fusion **47**, 2123–2143 (2005).

[7] L. Giannone, K. Mast, and M. Schubert, "Derivation of bolometer equations relevant to operation in fusion experiments," Rev. Sci. Instrum. **73**, 3205–3214 (2002).

[8] D. Zhang, R. Burhenn, R. Koenig, L. Giannone, P. A. Grodzki, B. Klein, K. Grosser, J. Baldzuhn, K. Ewert, V. Erckmann *et al.*, "Design criteria of the bolometer diagnostic for steady-state operation of the W7-X stellarator," Rev. Sci. Instrum. **81**, 10E134 (2010).

[9] G. A. Wurden, "A radiation-hard, steady state, digital imaging bolometer system," Fusion Eng. Des. **34–35**, 301–305 (1997).

[10] B. J. Peterson, "Infrared imaging video bolometer," Rev. Sci. Instrum. **71**(10), 3696–3701 (2000).

[11] R. Sano, K. Mukai, B. J. Peterson, M. Fukumoto, and K. Hoshino, "Conceptual design of imaging bolometer for use of computed tomography in JT-60SA," Rev. Sci. Instrum. **88**(5), 053506 (2017).

[12] J. Jang, B. J. Peterson, S. Oh, K. Mukai, S.-H. Hong, and W. Choe, "Reconstruction of radiation profiles near the plasma boundary using an infrared imaging video bolometer in KSTAR," Rev. Sci. Instrum. **89**(10), 10E111 (2018).

[13] J. Jang, W. Choe, B. J. Peterson, D. C. Seo, K. Mukai, R. Sano, S. Oh, S. H. Hong, J. Hong, and H. Y. Lee, "Tomographic reconstruction of two-dimensional radiated power distribution during impurity injection in KSTAR plasmas using an infrared imaging video bolometer," Curr. Appl. Phys. **18**(4), 461–468 (2018).

[14] S. Oh, J. Jang, and B. Peterson, "Radiation profile reconstruction of infrared imaging video bolometer data using a machine learning algorithm," Plasma Phys. Controlled Fusion **62**(3), 035014 (2020).

[15] F. Federici, M. L. Reinke, B. Lipschultz, A. J. Thornton, J. R. Harrison, J. J. Lovell, M. Bernert, and MAST Upgrade Team, "Design and implementation of a prototype infrared video bolometer (IRVB) in MAST Upgrade," Rev. Sci. Instrum. **94**(3), 033502 (2023).

[16] K. Mukai, B. J. Peterson, S. N. Pandya, R. Sano, and M. Itomi, "Improvement of infrared imaging video bolometer systems in LHD," Plasma Fusion Res. **9**, 3402037 (2014).

[17] B. J. Peterson, S. Konoshima, H. Parchamy, M. Kaneko, T. Omori, D. C. Seo, N. Ashikawa, and A. Sukegawa, "Observation of divertor and core radiation in JT-60U by means of bolometric imaging," J. Nucl. Mater. **363–365**, 412–415 (2007).

[18] S. P. Pandya, S. N. Pandya, Z. Shaikh, S. Shaikh, J. Govindarajan, and Aditya Team, "Development of infrared imaging video bolometer for the ADITYA tokamak," Plasma Fusion Res. **7**(1), 2402089 (2012).

[19] Z. Shaikh, S. P. Pandya, S. Shaikh, S. N. Pandya, and J. Govindarajan, "Development, calibration and performance testing of the infrared imaging video bolometer for the SST-1 Tokamak," in *27th PSSI National Symposium on Plasma Science and Technology on Challenges of Power Generation & Lighting 21st Century* (Excel India Publishers, 2013), pp. 431-434.

[20] M. L. Reinke, J. L. Terry, G. G. van Eden, B. J. Peterson, K. Mukai, T. K. Gray, and B. C. Stratton, "Experimental tests of an infrared video bolometer on Alcator C-Mod," Rev. Sci. Instrum. **89**(10), 103507 (2018).

[21] B. J. Peterson, S. Oh, D. Seo, J. Jang, J. S. Park, K. Mukai, and W. Choe, "Signal to noise ratio of upgraded imaging bolometer for KSTAR," Rev. Sci. Instrum. **89**(10), 10E115 (2018).

[22] A. Miyashita, K. Mukai, S. Ohshima, R. Matoike, B. J. Peterson, S. Kobayashi, H. Okada, S. Kado, T. Minami, T. Mizuuchi *et al.*, "First application of an infrared imaging video bolometer to Heliotron J plasma," Plasma Fusion Res. **16**, 1202079 (2021).

[23] N. Shigematsu, N. Ezumi, K. Mukai, T. Seto, T. Okamoto, K. Takanashi, S. Takahashi, R. Miyauchi, S. Togo, M. Hirata, J. Kohagura, M. Yoshikawa, R. Minami, Y. Nakashima, and M. Sakamoto, "Measurement of radiated power using an infrared imaging video bolometer system in the upstream of GAMMA 10/PDX divertor simulation plasma," Plasma Fusion Res. **18**, 2402031 (2023).

[24] B. J. Peterson, R. Sano, M. L. Reinke, J. M. Canik, L. F. Delgado-Aparicio, J. D. Lore, K. Mukai, T. K. Gray, G. G. van Eden, and M. A. Jaworski, "Preliminary design of a tangentially viewing imaging bolometer for NSTX-U," Rev. Sci. Instrum. **87**(11), 11D410 (2016).

[25] G. Partesotti, F. Reimold, G. A. Wurden, K. Mukai, B. J. Peterson, V. Winters, D. Zhang, and A. Demby, "Investigation of radiation distribution in W7-X with an infrared video bolometer camera," in Poster Contribution at FuseNet PhD Event, Lausanne, Switzerland, 2023.

[26] G. A. Wurden, L. A. Stephey, C. Biedermann, M. W. Jakubowski, J. P. Dunn, and M. Gamradt, "A high resolution IR/visible imaging system for the W7-X limiter," Rev. Sci. Instrum. **87**(11), 11D607 (2016).

[27] G. A. Wurden, C. Biedermann, F. Effenberg, M. Jakubowski, H. Niemann, L. Stephey, S. Bozhenkov, S. Brezinsek, J. Fellinger, B. Cannas *et al.*, "Limiter observations during W7-X first plasmas," Nucl. Fusion **57**(5), 056036 (2017).

[28] B. J. Peterson, G. Partesotti, F. Reimold, G. A. Wurden, Y. Gao, D. Zhang, V. Winters, M. Kobayashi, Y. Feng, K. Mukai, and J. von Miller, "Investigation of island size effect on radiation distribution during attached and detached plasmas in the island divertor of W7-X," Nucl. Mater. Energy **42**, 101868 (2025).

[29] M. Floristán, P. Müller, A. Gebhardt, A. Killinger, R. Gadow, A. Cardella, C. Li, R. Stadler, G. Zangl, M. Hirsch, H. P. Laqua, and W. Kasparek, "Development and testing of 140 GHz absorber coatings for the water baffle of W7-X cryopumps," Fusion Eng. Des. **86**(9–11), 1847–1850 (2011), part of Special Issue: Proceedings of the 26th Symposium of Fusion Technology (SOFT-26).

[30] D. Zhang, R. Burhenn, M. Hirsch, H. P. Laqua, R. König, J. W. Oosterbeek, J. Baldzuhn, P. A. Grodzki, K. Ewert, K. Grosser, and A. Cardella, "Suppression of high-power microwave impact onto diagnostic detectors during ECR-heating in fusion plasmas," in *38th EPS Conference on Plasma Physics 2011 (EPS 2011), Strasbourg, France, 27 June-1 July 2011* (Curran Associates, 2011), pp. 1548-1551.

[31] U. A. Sheikh, B. P. Duval, B. Labit, and F. Nespoli, "A novel carbon coating technique for foil bolometers," Rev. Sci. Instrum. **87**(11), 11D431 (2016).

[32] K. Mukai, R. Abe, B. J. Peterson, and S. Takayama, "Improvement of infrared imaging video bolometer for application to deuterium experiment on the large helical device," Rev. Sci. Instrum. **89**(10), 10E114 (2018).

[33] S. N. Pandya, B. J. Peterson, K. Mukai, R. Sano, A. Enokuchi, and N. Takeyama, "Improved signal to noise ratio and sensitivity of an infrared imaging video bolometer on large helical device by using an infrared periscope," Rev. Sci. Instrum. **85**(7), 073107 (2014).

[34] K. Mukai, T. Nishitani, K. Ogawa, and B. J. Peterson, "Neutron shielding design of infrared imaging video bolometer for LHD deuterium experiment," IEEE Trans. Plasma Sci. **47**(1), 18–21 (2019).

[35] G. Partesotti, F. Reimold, G. A. Wurden, B. J. Peterson, D. Zhang, and K. Mukai, "Assessing the toroidal radiation distribution at Wendelstein 7-X by combining Gaussian Process Tomography and field line mapping," Nucl. Mater. Energy **41**, 101823 (2024).

[36] S. Scott, H. James, F. Tom, C. Jordan, V. S. Sam, M. Jamie, M. Augustin, N. Emily, G. Christian, S. Mark, W. Alasdair, D. Rhys, K. Matt, and P. Artur (2024). "Calcam," Zenodo. https://doi.org/10.5281/zenodo.10655746

[37] D. Zhang, R. Burhenn, C. D. Beidler, Y. Feng, H. Thomsen, C. Brandt, S. Buller, F. Reimold, P. Hacker, R. Laube *et al.*, "Bolometer tomography on Wendelstein 7-X for study of radiation asymmetry," Nucl. Fusion **61**(11), 116043 (2021).

[38] B. J. Peterson, R. Reichle, S. Pandya, M. G. O'Mullane, and K. Mukai, "Consideration of signal to noise ratio for an imaging bolometer for ITER," Rev. Sci. Instrum. **92**(4), 043534 (2021).

[39] G. Partesotti, F. Reimold, J. Ruhnau, A. Tsikouras, D. Kubeneck, D. Zhang, P. Geißler, and W7-X Team, "Development of a compact bolometer camera concept for investigation of radiation asymmetries at Wendelstein 7-X," Rev. Sci. Instrum. **95**(10), 103503 (2024).

[40] T. Andreeva, J. Geiger, A. Dinklage, G. Wurden, H. Thomsen, K. Rahbarnia, J. C. Schmitt, M. Hirsch, G. Fuchert, C. Nührenberg *et al.*, "Magnetic configuration scans during divertor operation of Wendelstein 7-X," Nucl. Fusion **62**(2), 026032 (2022).

[41] J. Lovell, G. Naylor, A. Field, P. Drewelow, R. Sharples, and J. Contributors, "An FPGA-based bolometer for the MAST-U Super-X divertor," Rev. Sci. Instrum. **87**(11), 11E721 (2016).

[42] J. Lovell, "Development of smart, compact fusion diagnostics using field-programmable gate arrays," Ph.D. dissertation (Durham University, 2017).

[43] H. P. Araghy, B. J. Peterson, H. Hayashi, S. Konoshima, N. Ashikawa, and D. Seo, "Spatial variation of the foil parameters from in situ calibration of the JT-60U imaging bolometer foil," Plasma Fusion Res. **2**, S1116 (2007).

[44] R. Sano, B. J. Peterson, E. A. Drapiko, Y. Watanabe, Y. Yamauchi, and T. Hino, "Thermal characteristics of foils for an imaging bolometer," Plasma Fusion Res. **6**, 2406076 (2011).

[45] R. Sano, B. J. Peterson, E. A. Drapiko, D. Seo, Y. Yamauchi, and T. Hino, "Foil calibration for IR imaging bolometer by laser irradiation," Plasma Fusion Res. **7**, 2405039 (2012).

[46] S. N. Pandya, B. J. Peterson, R. Sano, K. Mukai, E. A. Drapiko, A. G. Alekseyev, T. Akiyama, M. Itomi, and T. Watanabe, "Calibration of a thin metal foil for infrared imaging video bolometer to estimate the spatial variation of thermal diffusivity using a photo-thermal technique," Rev. Sci. Instrum. **85**(5), 054902 (2014).

[47] B. J. Peterson, A. Y. Kostrioukov, N. Ashikawa, M. Osakabe, and S. Sudo, "Calibration and sensitivity of the infrared imaging video bolometer," Rev. Sci. Instrum. **74**(3), 2040–2043 (2003).

[48] H. Parchamy, B. J. Peterson, S. Konoshima, H. Hayashi, D. C. Seo, and N. Ashikawa, "Detailed *in situ* laser calibration of the infrared imaging video bolometer for the JT-60U tokamak," Rev. Sci. Instrum. **77**(10), 10E515 (2006).

[49] K. Mukai, B. J. Peterson, S. N. Pandya, and R. Sano, "*In situ* calibration of an infrared imaging video bolometer in the Large Helical Device," Rev. Sci. Instrum. **85**(11), 11E435 (2014).

[50] G. A. Wurden, G. Partesotti, F. Reimold, K. Mukai, B. J. Peterson, and F. Federici, "Developing a robust sensor for infrared imaging bolometers," Rev. Sci. Instrum. **95**(9), 093503 (2024).

[51] F. Federici, J. J. Lovell, G. A. Wurden, B. J. Peterson, and K. Mukai, "Increased accuracy and signal-to-noise ratio through recent improvements in infra-red video bolometer fabrication and calibration," Rev. Sci. Instrum. **95**(10), 103525 (2024).

[52] T. Wegner, B. Geiger, F. Kunkel, R. Burhenn, T. Schröder, C. Biedermann, B. Buttenschön, G. Cseh, P. Drews, O. Grulke *et al.*, "Design, capabilities, and first

results of the new laser blow-off system on Wendelstein 7-X," Rev. Sci. Instrum. **89**(7), 073505 (2018).

[53] S. N. Pandya, B. J. Peterson, M. Kobayashi, S. P. Pandya, K. Mukai, and R. Sano, "A reconsideration of the noise equivalent power and the data analysis procedure for the infrared imaging video bolometers," Rev. Sci. Instrum. **85**(12), 123501 (2014).

[54] M. Jakubowski, M. Endler, Y. Feng, Y. Gao, C. Killer, R. König, M. Krychowiak, V. Perseo, F. Reimold, O. Schmitz *et al.*, "Overview of the results from divertor experiments with attached and detached plasmas at Wendelstein 7-X and their implications for steady-state operation," Nucl. Fusion **61**(10), 106003 (2021).

[55] B. J. Peterson, E. A. Drapiko, D. Seo, and N. Ashikawa, "Comparison of Au and Pt foils for an imaging bolometer," Plasma Fusion Res. **5**, 035 (2010).

[56] Y. Gao, M. W. Jakubowski, P. Drewelow, F. Pisano, A. Puig Sitjes, H. Niemann, A. Ali, B. Cannas, and W7-X Team, "Methods for quantitative study of divertor heat loads on W7-X," Nucl. Fusion **59**(6), 066007 (2019).

[57] G. Partesotti, F. Reimold, A. Tsikouras, D. Zhang, G. Kawamura, B. J. Peterson, and W7-X Team, "Improved weighted sum estimation of total radiated power at W7-X," Nucl. Fusion **65**(1), 016035 (2024).